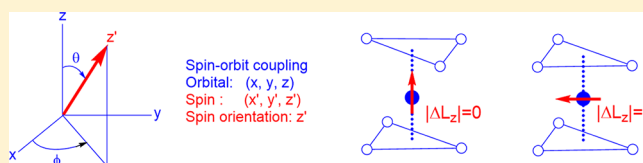


Electronic and Structural Factors Controlling the Spin Orientations of Magnetic Ions

Myung-Hwan Whangbo,^{*,†,‡,§,||} Hongjun Xiang,^{||,⊥} Hyun-Joo Koo,[#] Elijah E. Gordon,[¶] and Jerry L. Whitten[†][†]Department of Chemistry, North Carolina State University, Raleigh, North Carolina 27695-8204, United States[‡]State Key Laboratory of Structural Chemistry, Fujian Institute of Research on the Structure of Matter, Chinese Academy of Sciences, Fuzhou 350002, P. R. China[§]State Key Laboratory of Crystal Materials, Shandong University, Jinan 250100, P. R. China^{||}Key Laboratory of Computational Physical Sciences (Ministry of Education), State Key Laboratory of Surface Physics, and Department of Physics, Fudan University, Shanghai 200433, P. R. China[⊥]Collaborative Innovation Center of Advanced Microstructures, Nanjing 210093, P. R. China[#]Department of Chemistry and Research institute for Basic Sciences, Kyung Hee University, Seoul 02447, Republic of Korea[¶]Ames Laboratory, U.S. Department of Energy, Ames, Iowa 50011, United States

ABSTRACT: Magnetic ions M in discrete molecules and extended solids form ML_n complexes with their first-coordinate ligand atoms L . The spin moment of M in a complex ML_n prefers a certain direction in coordinate space because of spin-orbit coupling (SOC). In this minireview, we examine the structural and electronic factors governing the preferred spin orientations. Elaborate experimental measurements and/or sophisticated computational efforts are required to find the preferred spin orientations of magnetic ions, largely because the energy scale of SOC is very small. The latter is also the very reason why one can readily predict the preferred spin orientation of M by analyzing the SOC-induced highest occupied molecular orbital (HOMO)–lowest unoccupied molecular orbital (LUMO) interactions of the ML_n complexes in terms of qualitative perturbation theory. The strength of this HOMO–LUMO interaction depends on the spin orientation, which is governed by the selection rules based on the minimum $|\Delta L_z|$ value (i.e., the minimum difference in the magnetic quantum numbers) between the HOMO and LUMO. With the local z axis of ML_n chosen as its n -fold rotational axis, the preferred spin orientation is parallel to the z axis ($\parallel z$) when $|\Delta L_z| = 0$ but perpendicular to the z axis ($\perp z$) when $|\Delta L_z| = 1$.



1. INTRODUCTION

Transition-metal magnetic ions M in magnetic solids and discrete molecules form ML_n (typically, $n = 2$ –6) “complexes” with their first-coordinate ligand atoms L . With the n -fold ($n \geq 3$) rotational axis of ML_n taken as the local z axis, the magnetic moment associated with the unpaired spins of ML_n is typically parallel to the z axis (the $\parallel z$ direction) or perpendicular to the z axis (the $\perp z$ direction). For example, the high-spin Fe^{2+} (d^6 , $S = 2$) ion adopts the $\parallel z$ spin orientation in linear molecules $Fe[C(SiMe_3)_3]_2^{1-5}$ and $Fe[N(t-Bu)_2]_2^6$ (Figure 1a). The high-spin Ni^{2+} (d^8 , $S = 1$) ions of the NiO_6 trigonal prisms show the $\perp z$ spin orientation (Figure 1b) in 2H-perovskite $Sr_3NiPtO_6^{7,8}$ but the $\parallel z$ spin orientation (Figure 1c) in the isostructural phase $Sr_3NiIrO_6^{8-10}$. The $\parallel z$ spin orientation is also found for the high-spin Co^{2+} (d^7 , $S = 3/2$) ions in the CoO_6 trigonal prisms of 2H-perovskites $Ca_3CoMnO_6^{11,12}$, $Ca_3CoPtO_6^{7,13}$ and $Sr_3CoPtO_6^{7,13}$ as well as the high-spin Rh^{2+} (d^7 , $S = 3/2$) ions in the RhO_6 trigonal prisms of 2H-perovskites $Sr_4RhO_6^{7,13}$ and $Sr_3CaRhO_6^{7,13}$. The high-spin Mn^{3+} (d^4 , $S = 2$) ion of the axially elongated MnO_6 octahedra in $TbMnO_3^{14,15}$ and $Ag_2MnO_2^{16,17}$ adopts the $\parallel z$ spin orientation

(Figure 1d), and the low-spin Ir^{4+} (d^5 , $S = 1/2$) ion of the axially elongated IrO_6 octahedron in Sr_2IrO_4 has the $\perp z$ spin orientation (Figure 1e).^{8,18,19} The low-spin Ir^{4+} (d^5 , $S = 1/2$) ions are parallel to the 3-fold rotational axis of the IrO_6 octahedra in 2H-perovskites $Sr_3NiIrO_6^{8-10}$, $Sr_4IrO_6^{7,13}$, $Sr_3CaIrO_6^{7,13}$ and Ca_4IrO_6 (Figure 1f).^{7,13} Such a spin orientation is also found for the Mn^{4+} (d^3 , $S = 3/2$) ions of the MnO_6 octahedra in $Ca_3CoMnO_6^{11,12}$ and the high-spin Fe^{2+} (d^6 , $S = 2$) ions of the FeO_6 octahedra in $BaFe_2(PO_4)_2^{20,21}$. The $\parallel z$ spin orientation is preferred for the Cu^{2+} (d^9 , $S = 1/2$) ion of the CuN_4 square plane in the discrete molecule $Cu(NH_3)_4SO_4 \cdot H_2O^{22,23}$ and the CuO_4 square plane of $Sr_3CuPtO_6^{24}$ (Figure 1g), but the $\perp z$ spin orientation is preferred in the CuL_4 square plane of the CuL_2 ($L = Cl, Br, O$) ribbon chains^{25–28} and $CuCl_2 \cdot 2H_2O^{29–31}$

Special Issue: Paradigm Shifts in Magnetism: From Molecules to Materials

Received: March 9, 2019

Published: June 18, 2019



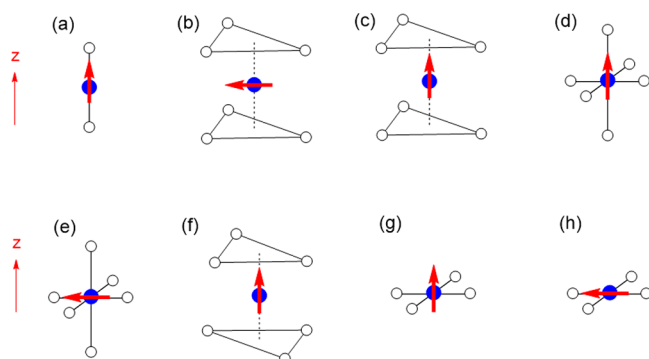


Figure 1. Spin orientations observed for various magnetic ions in ML_n complexes: (a) high-spin Fe^{2+} (d^6 , $S = 2$) ion of linear ML_2 ; (2) high-spin Ni^{2+} (d^8 , $S = 1$) ion of the NiO_6 trigonal prism in Sr_3NiPtO_6 ; (c) high-spin Ni^{2+} (d^8 , $S = 1$) ion of the NiO_6 trigonal prism in Sr_3NiIrO_6 ; (d) high-spin Mn^{3+} (d^4 , $S = 2$) ion of the axially elongated MnO_6 octahedron in $TbMnO_3$; (e) low-spin Ir^{4+} (d^5 , $S = 1/2$) ion of the axially elongated IrO_6 octahedron in Sr_3IrO_4 ; (f) low-spin Ir^{4+} (d^5 , $S = 1/2$) ion of the IrO_6 octahedron in Sr_3NiIrO_6 ; (g) Cu^{2+} (d^9 , $S = 1/2$) ion of the isolated CuN_4 square plane in $Cu(NH_3)_4SO_4 \cdot H_2O$; (h) Cu^{2+} (d^9 , $S = 1/2$) ion of the CuL_4 square plane in CuL_2 ($L = Cl, Br$) ribbons in which CuL_4 square planes share their opposite edges.

(Figure 1h). The $\perp z$ spin orientation is also found for the high-spin Fe^{2+} (d^6 , $S = 2$) ion in the FeO_4 square planes of $SrFeO_2$ ^{32,33} and $Sr_3Fe_2O_5$.^{34,35} Numerous studies have been carried out to search for the conceptual tools that enable one to understand and think about these experimental/theoretical findings by focusing on the question of how the preferred spin orientations of ML_n complexes are related to the interactions between their occupied and unoccupied d states under the action of spin–orbit coupling (SOC).^{8,15,17,31,33,35–38} These efforts have led to the simple selection rules with which one can readily predict the preferred spin directions of ML_n complexes by analyzing their SOC-induced highest occupied molecular orbital (HOMO)–lowest unoccupied molecular orbital (LUMO) interactions in terms of qualitative perturbation theory.³⁶

The magnetic ion M of a given ML_n complex is characterized by the spin and orbital angular momenta \vec{S} and \vec{L} , respectively. It is the SOC $\lambda \vec{S} \cdot \vec{L}$ that determines the preferred spin orientation of M . To analyze what electronic factors of ML_n are responsible for their preferred spin orientations, it is necessary to discuss the SOC by using two independent coordinate systems (Figure 2): one coordinate system (x, y, z) for \vec{L} and another coordinate system (x', y', z') for \vec{S} .²³ Then, the z' -axis direction is the preferred spin orientation, which is defined by the polar angles (θ, ϕ) with respect to the (x, y, z) coordinate system. The $\parallel z$ spin orientation (i.e., the easy-axis magnetic anisotropy) occurs when $\theta = 0^\circ$, while the $\perp z$ spin orientation (i.e., the easy-plane magnetic anisotropy) occurs when $\theta = 90^\circ$. The preferred spin orientations are observed directly by neutron diffraction measurements on a single crystal or on polycrystalline powder samples and are inferred indirectly by techniques such as electron paramagnetic resonance and magnetic torque measurements on single crystals. Computationally, the preferred spin orientation of ML_n is determined by first-principles density functional theory (DFT) calculations including SOC. On the qualitative level, one can readily predict the preferred spin orientations of ML_n

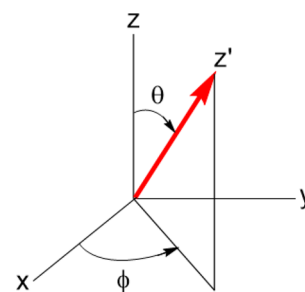


Figure 2. Use of the two independent coordinate systems in describing the SOC $\lambda \vec{S} \cdot \vec{L}$: (x, y, z) for \vec{L} and (x', y', z') for \vec{S} .

by employing the perturbation theory with SOC taken as perturbation, namely, by considering the SOC-induced interaction between the HOMO and LUMO of ML_n . The primary reason for this seemingly surprising result is that the effect of SOC in determining the preferred spin orientation is very small in the energy scale compared with the d-state splitting of ML_n .

The small energy scale of SOC has an important consequence in that the preferred spin direction determined by SOC can be overridden or modified by stronger interactions involving the spins such as spin exchanges between adjacent spins.⁸ Upon lowering of the temperature, a magnetic solid consisting of identical magnetic ions may undergo a long-range magnetic ordering to a noncollinear superstructure (e.g., a cycloid or a helix depicted in Figure 3a,b) at a certain temperature in the case when its spin exchange interactions are not strongly spin-frustrated.^{15,17,37–41} Prior to reaching this temperature, such a

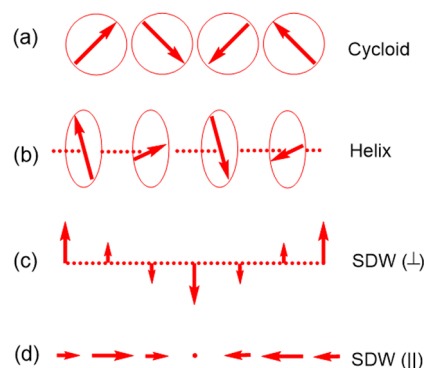


Figure 3. Magnetic superstructures of certain magnetic solids made up of identical magnetic ions observed when lowering the temperature: (a) a cycloid; (b) a helix; (c) a transverse SDW; (d) a longitudinal SDW.

magnetic solid commonly undergoes another phase transition, i.e., a transverse or a longitudinal spin-density wave (SDW; Figure 3c,d).^{42–47} In a cycloid or a helix, the spin moment at every magnetic ion site has an identical magnitude, but its orientation changes depending on the position of the magnetic ion. In a SDW, however, the magnitudes of the spin moments at magnetic ion sites vary sinusoidally depending on their positions as if the magnetic system consists of magnetic ions with different magnetic moments despite the fact that it is made up of identical magnetic ions. The key to resolving this apparent puzzle is that a cycloid or a helix is chiral, and there are two chiral structures of opposite chirality that are identical in energy and hence are equally probable at a given temperature.⁴⁸

The main objective of this article is to survey the theoretical conceptual tools with which to think about the preferred spin directions of magnetic ions in magnetic solids and discrete molecules. Over the years, they were developed and discussed in a number of articles^{8,15,17,31,33,35} and reviews.^{23,36–38} This survey is written with the objective of providing a self-contained description and the expectation that the qualitative concepts summarized here will help to predict the preferred spin directions of magnetic systems based solely on their crystal structures before launching elaborate experimental measurements or theoretical calculations to determine them.

Our work is organized as follows: The important properties of orbital and spin angular momenta are discussed in section 2 and those of the SOC in section 3. Section 4 examines the cause for uniaxial magnetism from the viewpoint of the one electron and the first-principles picture. In section 5, we discuss the selection rules for predicting the preferred spin directions and analyze various examples of preferred spin orientations. In section 6, we discuss how the preferred spin orientation of a given magnetic ion M, determined by SOC, is modified by the spin exchanges of M with its adjacent magnetic ions. Finally, our concluding remarks are given in section 7.

2. ORBITAL AND SPIN ANGULAR MOMENTA

2.1. Angular Behaviors of Atomic Orbitals. The angular properties of atomic orbitals are characterized by the spherical harmonics $|L, L_z\rangle$, which are determined by the orbital quantum number L and the magnetic quantum numbers L_z . These functions (hereafter referred to as orbital states) enable one to evaluate how atomic orbitals are affected by angular momentum operators. For a given L , there are $2L + 1$ orbital states $|L, L_z\rangle$, where $L_z = -L, -L + 1, \dots, L - 1, L$, for example, $|2, -2\rangle, |2, -1\rangle, |2, 0\rangle, |2, +1\rangle$, and $|2, +2\rangle$ for d orbitals and $|1, -1\rangle, |1, 0\rangle$, and $|1, +1\rangle$ for p orbitals. In terms of the orbital states, the angular properties of the d orbitals are summarized in Table 1, where the angular behaviors of the f orbitals in terms of the orbital states $|3, -3\rangle, |3, -2\rangle, |3, -1\rangle, |3, 0\rangle, |3, +1\rangle, |3, +2\rangle$, and $|3, +3\rangle$ are also given. For simplicity, we use the convention that the p_x, p_y , and p_z orbitals are referred to as the x, y , and z orbitals, respectively, and the $d_{3z^2-r^2}, d_{xz}, d_{yz}, d_{xy}$, and $d_{x^2-y^2}$ orbitals as the $3z^2 - r^2, xz, yz, xy$, and $x^2 - y^2$ orbitals, respectively (Figure 4). In our discussion, the split d states of ML_n are described as if they are solely composed of the d orbitals of M. This is done only for convenience under the understanding that, in the d states, the d orbitals of M are combined out-of-phase with the p orbitals of L.

According to the L_z values, the d orbitals can be grouped into three sets, namely, $L_z = 0$ for $\{3z^2 - r^2\}$, $L_z = \pm 1$ for $\{xz, yz\}$, and $L_z = \pm 2$ for $\{xy, x^2 - y^2\}$. Similarly, the p orbitals can be grouped into two sets, $L_z = 0$ for $\{z\}$, and $L_z = \pm 1$ for $\{x, y\}$. Thus, the minimum difference in the magnetic quantum numbers, $|\Delta L_z|$, is 1 between $\{3z^2 - r^2\}$ and $\{xz, yz\}$, between $\{xz, yz\}$ and $\{xy, x^2 - y^2\}$, and between $\{z\}$ and $\{x, y\}$. $|\Delta L_z| = 0$ between the different members of the sets $\{xz, yz\}$, $\{xy, x^2 - y^2\}$, and $\{x, y\}$. $|\Delta L_z| = 2$ between $\{3z^2 - r^2\}$ and $\{xy, x^2 - y^2\}$. These relationships are summarized in Figure 5.^{36,38} Similar relationships can be readily established for the f orbitals.

2.2. Orbital Angular Momentum and Orbital Quenching.²³ The magnetic properties of a magnetic ion are characterized by its orbital and spin angular momenta, \vec{L} and \vec{S} , respectively. These angular momenta interact with an external

Table 1. Angular Properties of Atomic p, d, and f Orbitals

z/r	$ 1, 0\rangle$
x/r	$\frac{1}{\sqrt{2}}(1, -1\rangle - 1, +1\rangle)$
y/r	$i\frac{1}{\sqrt{2}}(1, -1\rangle + 1, +1\rangle)$
$(3z^2 - r^2)/r^2$	$ 2, 0\rangle$
xz/r^2	$\frac{1}{\sqrt{2}}(2, -1\rangle - 2, +1\rangle)$
yz/r^2	$i\frac{1}{\sqrt{2}}(2, -1\rangle + 2, +1\rangle)$
xy/r^2	$i\frac{1}{\sqrt{2}}(2, -2\rangle - 2, +2\rangle)$
$(x^2 - y^2)/r^2$	$\frac{1}{\sqrt{2}}(2, -2\rangle + 2, +2\rangle)$
z^3/r^3	$ 3, 0\rangle$
xz^2/r^3	$\frac{1}{\sqrt{2}}(3, -1\rangle - 3, +1\rangle)$
yz^2/r^3	$i\frac{1}{\sqrt{2}}(3, -1\rangle + 3, +1\rangle)$
$(x^2 - y^2)z/r^3$	$\frac{1}{\sqrt{2}}(3, -2\rangle + 3, +2\rangle)$
xyz/r^3	$i\frac{1}{\sqrt{2}}(3, -2\rangle - 3, +2\rangle)$
$x(x^2 - 3y^2)/r^3$	$\frac{1}{\sqrt{2}}(3, -3\rangle - 3, +3\rangle)$
$y(3x^2 - y^2)/r^3$	$i\frac{1}{\sqrt{2}}(3, -3\rangle + 3, +3\rangle)$

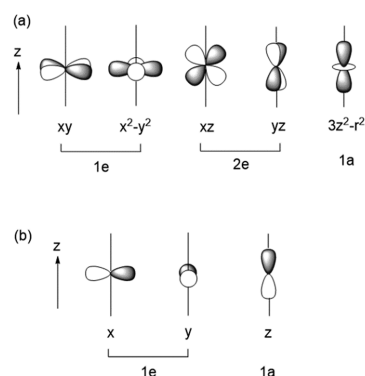


Figure 4. Shapes of the atomic (a) d orbitals and (b) p orbitals of the magnetic ion M of ML_n , where the z axis refers to the n -fold rotational axis of ML_n .

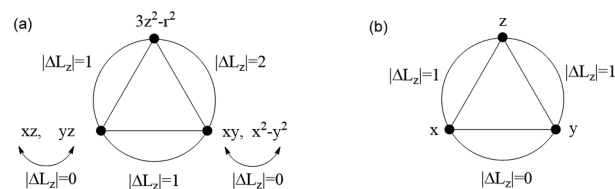


Figure 5. Values of the minimum difference $|\Delta L_z|$ in the magnetic quantum numbers between different members of the orbital states $|L, L_z\rangle$: (a) between d states; (b) between p states.

magnetic field, leading to the Zeeman interaction, or with each other, leading to SOC. In the description of these interactions, it is

necessary to consider the angular momenta \vec{L} and \vec{S} as quantum-mechanical operators \hat{L} and \hat{S} , respectively, as will be discussed below.

The orbital magnetic moment $\vec{\mu}_L$ of a magnetic ion is related to how strongly its total energy E changes by the applied magnetic field \vec{H} , namely²³

$$\vec{\mu}_L = -\frac{\partial E}{\partial \vec{H}} \quad (1)$$

and to its orbital angular momentum \vec{L} as $\vec{\mu}_L = -\mu_B \vec{L}$, where μ_B is the Bohr magneton. Thus, the orbital angular momentum relates the field-induced change in the energy to the applied magnetic field as

$$\vec{L} = \frac{\partial E}{\mu_B \partial \vec{H}} \quad (2)$$

A similar expression is valid for the spin magnetic moment $\vec{\mu}_S = -2\mu_B \vec{S}$ and for the total magnetic moment $\vec{\mu}_{\text{tot}} = \vec{\mu}_L + \vec{\mu}_S = -\mu_B(\vec{L} + 2\vec{S})$. In a quantum-mechanical description, the magnetic moment of a system is related to whether its ground doublet is split in energy by a magnetic field applied along a certain direction; it has no magnetic moment along that direction if the degeneracy of the doublet state is not lifted under the magnetic field (see section 4.1).

The energy scale associated with the angular momentum of a magnetic ion is very small relative to that associated with the chemical bonding, the geometry distortion, or the SOC involving the magnetic ion. For instance, the magnetic field H of 1 T is equal to the $\mu_B H$ value of 0.058 meV, which is 0.67 K. Note that 1 meV = 11.6 K, so raising the magnetic field by 1 T is equivalent to raising the temperature by 0.67 K. This small energy scale is the primary cause for the orbital momentum quenching for most magnetic ions. To illustrate this point, we consider a magnetic ion that has a single electron so that its total energy is equal to the energy of its occupied orbital. The energy of a magnetic ion with the orbital angular momentum \vec{L} under the magnetic field \vec{H} is described by the Zeeman interaction H_Z . If the field is applied along the z direction,

$$H_Z = \mu_B \vec{L} \cdot \vec{H} = \mu_B L_z H_z \quad (3)$$

Using the effective one-electron Hamiltonian \hat{H}^{eff} for this system, we have

$$\hat{H}^{\text{eff}}|i\rangle = \varepsilon_i|i\rangle \quad (i = x, y, z) \quad (4)$$

where ε_x , ε_y , and ε_z are the energies of the p states $|x\rangle$, $|y\rangle$, and $|z\rangle$, respectively. Under the magnetic field \vec{H} , the energy of this system is given by the Hamiltonian $\hat{H} = \hat{H}^{\text{eff}} + \hat{H}_Z$, where $\hat{H}_Z = \mu_B \hat{L}_z$, so that

$$\hat{H} = \hat{H}^{\text{eff}} + \mu_B \hat{L}_z \quad (5)$$

where \hat{L}_z is the operator corresponding to the orbital angular momentum L_z (see section 2.2). Then, the matrix representation $\langle i|\hat{H}|j\rangle$ ($i, j = x, y, z$) of \hat{H} in terms of the three p states is written as (see Table 2)

$$\begin{pmatrix} \langle x|\hat{H}|x\rangle & \langle x|\hat{H}|y\rangle & \langle x|\hat{H}|z\rangle \\ \langle y|\hat{H}|x\rangle & \langle y|\hat{H}|y\rangle & \langle y|\hat{H}|z\rangle \\ \langle z|\hat{H}|x\rangle & \langle z|\hat{H}|y\rangle & \langle z|\hat{H}|z\rangle \end{pmatrix} = \begin{pmatrix} \varepsilon_x & -i\mu_B H_z & 0 \\ i\mu_B H_z & \varepsilon_y & 0 \\ 0 & 0 & \varepsilon_z \end{pmatrix} \quad (6)$$

Table 2. Nonzero Integrals of the Angular Momentum Operators $\langle i|\hat{L}_x|j\rangle$, $\langle i|\hat{L}_y|j\rangle$, and $\langle i|\hat{L}_z|j\rangle$ ($i, j = x, y, z$ or $i, j = 3z^2 - r^2, xz, yz, x^2 - y^2, xy$)

\hat{L}_z	$\langle y \hat{L}_z x\rangle = i$
\hat{L}_x	$\langle z \hat{L}_x y\rangle = i$
\hat{L}_y	$\langle x \hat{L}_y z\rangle = i$
\hat{L}_z	$\langle xy \hat{L}_z x^2 - y^2\rangle = 2i$
	$\langle xz \hat{L}_z yz\rangle = -i$
\hat{L}_x	$\langle 3z^2 - r^2 \hat{L}_x yz\rangle = i\sqrt{3}$
	$\langle x^2 - y^2 \hat{L}_x yz\rangle = i$
	$\langle xz \hat{L}_x xy\rangle = i$
\hat{L}_y	$\langle 3z^2 - r^2 \hat{L}_y xz\rangle = -i\sqrt{3}$
	$\langle x^2 - y^2 \hat{L}_y xz\rangle = i$
	$\langle yz \hat{L}_y xy\rangle = -i$

By diagonalizing this matrix, one obtains the three energy levels

$$\begin{aligned} E_1 &= \frac{(\varepsilon_x + \varepsilon_y) - \sqrt{(\varepsilon_x - \varepsilon_y)^2 + 4\mu_B^2 H_z^2}}{2} \\ E_2 &= \frac{(\varepsilon_x + \varepsilon_y) + \sqrt{(\varepsilon_x - \varepsilon_y)^2 + 4\mu_B^2 H_z^2}}{2} \\ E_3 &= \varepsilon_z \end{aligned} \quad (7)$$

There are two possible cases for the ground state.

(a) If $E_3 < E_1$, the energy of the ground state is E_3 . Because E_3 is independent of the applied field, the magnetic moment of the system is zero, so $L_z = 0$.

(b) If $E_1 < E_3$, the energy of the ground state is E_1 because $E_1 < E_2$. Thus, the orbital angular momentum of the electron becomes

$$L_z = \frac{\partial E_1}{\mu_B \partial H_z} = \frac{-2\mu_B H_z}{\sqrt{(\varepsilon_x - \varepsilon_y)^2 + 4\mu_B^2 H_z^2}} \quad (8)$$

so the L_z value becomes -1 (in \hbar units) when the $|x\rangle$ and $|y\rangle$ levels are degenerate (i.e., $\varepsilon_x = \varepsilon_y$). The latter happens when the site of the magnetic ion has an n -fold ($n \geq 3$) rotational symmetry around the z axis. Otherwise, the degeneracy of the $|x\rangle$ and $|y\rangle$ levels is lifted so $\varepsilon_x \neq \varepsilon_y$. To illustrate the nature of the orbital momentum quenching, we consider the case of a very small energy difference of $|\varepsilon_x - \varepsilon_y|$, e.g., 1 meV. This is a representative case when $|x\rangle$ and $|y\rangle$ are nondegenerate by symmetry but are practically degenerate in terms of their energies. This energy difference is still much greater than the magnetic energy $\mu_B H_z$ even at a large magnetic field of 1 T (i.e., 0.058 meV), so that $\mu_B H_z \ll |\varepsilon_x - \varepsilon_y|$. Consequently, eq 8 becomes

$$L_z \approx -\frac{2\mu_B H_z}{|\varepsilon_x - \varepsilon_y|} \quad (9)$$

so $|L_z| \ll 1$. This example shows why orbital momentum quenching (i.e., $\vec{L} \approx 0$) takes place for most magnetic ions in

solids and molecules. Because of the orbital momentum quenching, their total moments $\vec{\mu}_{\text{tot}} = \vec{\mu}_L + \vec{\mu}_S = -\mu_B(\vec{L} + 2\vec{S})$ are well approximated by their spin moments, $\vec{\mu}_{\text{tot}} \approx -2\mu_B\vec{S}$.

Quenching of the orbital momentum does not occur for a magnetic ion with electron configuration possessing an unevenly occupied degenerate level (e.g., one electron in a triply degenerate level discussed above; one or three electrons in a doubly degenerate d level). Such a magnetic ion has uniaxial magnetism, namely, its magnetic moment is nonzero only along the direction of the rotational axis responsible for generation of the degenerate states. Such a magnetic ion is susceptible to a Jahn–Teller (JT) distortion,^{12,23} which lowers the symmetry of the ion site, thereby lifting the degeneracy of the level and, consequently, destroying the uniaxial magnetism. Thus, a magnetic ion can exhibit uniaxial magnetism only when its JT instability is removed, typically by having sterically bulky ligands around the magnetic ion.^{3,6} To explain uniaxial magnetism, one needs to know how the L_z values of the orbital states $|L, L_z\rangle$ defining the angular properties of the atomic p and d orbitals are affected by the angular momentum operators. This will then allow us to discuss the SOC and why a magnetic ion possessing an unevenly occupied degenerate level exhibits uniaxial magnetism.

2.3. Angular Momentum Operators. In a quantum-mechanical description, the orbital angular momentum \vec{L} is replaced by the orbital angular momentum operator \hat{L} that has the Cartesian components $(\hat{L}_x, \hat{L}_y, \hat{L}_z)$. Most calculations associated with the angular momentum operators employ the set $(\hat{L}_z, \hat{L}_+, \hat{L}_-)$, where the ladder operators \hat{L}_{\pm} are defined by $\hat{L}_{\pm} = \hat{L}_x \pm i\hat{L}_y$. The orbital states $|L, L_z\rangle$ are affected by these operators as follows:

$$\begin{aligned}\hat{L}_z|L, L_z\rangle &= L_z|L, L_z\rangle \\ \hat{L}_{\pm}|L, L_z\rangle &= \sqrt{L(L+1) - L_z(L_z \pm 1)}|L, L_z \pm 1\rangle\end{aligned}\quad (10)$$

Similarly, the spin angular momentum \vec{S} is replaced by the spin angular momentum operator \hat{S} , which has the Cartesian components $(\hat{S}_x, \hat{S}_y, \hat{S}_z)$. The magnetic ion with total spin S is described by a set of spin states $|S, S_z\rangle$, where S_z takes $2S + 1$ values, namely, $S_z = -S, -S + 1, \dots, S - 1, S$. Calculations associated with the spin angular momentum operators make use of the set $(\hat{S}_z, \hat{S}_+, \hat{S}_-)$, where the ladder operators \hat{S}_{\pm} are defined by $\hat{S}_{\pm} = \hat{S}_x \pm i\hat{S}_y$. The spin states $|S, S_z\rangle$ are affected by these operators as follows:

$$\begin{aligned}\hat{S}_z|S, S_z\rangle &= S_z|S, S_z\rangle \\ \hat{S}_{\pm}|S, S_z\rangle &= \sqrt{S(S+1) - S_z(S_z \pm 1)}|S, S_z \pm 1\rangle\end{aligned}\quad (11)$$

Note that the \hat{L}_z operator does not change the L_z value of $|L, L_z\rangle$, but the ladder operators \hat{L}_{\pm} change it by ± 1 (eq 10). Similarly, the \hat{S}_z operator does not change the S_z value of $|S, S_z\rangle$, but the ladder operators \hat{S}_{\pm} change it by ± 1 (eq 11). Therefore, the evaluation of the integrals such as $\langle L, L_z' | \hat{L}_{\mu} | L, L_z \rangle$ and $\langle S, S_z' | \hat{S}_{\mu} | S, S_z \rangle$ comes down to recognizing the orthonormality of the orbital and spin states

$$\begin{aligned}\langle L, L_z' | L, L_z \rangle &= \delta_{L_z' L_z} \\ \langle S, S_z' | S, S_z \rangle &= \delta_{S_z' S_z}\end{aligned}\quad (12)$$

From eqs 10–12, the nonzero integrals $\langle i | \hat{L}_{\mu} | j \rangle$ ($\mu = +, -, z$) involving atomic p orbitals ($i, j = x, y, z$) and those involving

atomic d orbitals ($i, j = 3z^2 - r^2, xz, yz, x^2 - y^2, xy$) can be readily determined (Table 2).

In the literature, the orbital and spin angular momenta are used as quantum-mechanical operators (i.e., \hat{L} and \hat{S}) in discussing SOC and Zeeman interactions but as classical vectors (i.e., \vec{L} and \vec{S}) in discussing all other aspects. This practice will be followed in our discussion.

3. SOC²³

In classical mechanics, the orbital and spin angular momenta (\vec{L} and \vec{S} , respectively) of a magnetic ion are treated as vectors, so the SOC between them is described by

$$E_{\text{SO}} = \lambda \vec{S} \cdot \vec{L} \quad (13)$$

where λ is the SOC constant. The λ value of a magnetic ion increases with increasing atomic number and increasing oxidation state. If the electron shell with unpaired electrons is less than half-occupied, e.g., V^{4+} ($d^1, S = 1/2$), λ is positive so the lowest energy of E_{SO} occurs when \vec{L} and \vec{S} are antiparallel. If the shell is more than half-occupied, e.g., Cu^{2+} ($d^9, S = 1/2$), λ is negative so the lowest energy of E_{SO} occurs when \vec{L} and \vec{S} are parallel. If the shell of a magnetic ion is half-occupied (e.g., high-spin Mn^{2+} and Fe^{3+} with $d^5, S = 5/2$), its SOC is expected to vanish ($E_{\text{SO}} = 0$) because, formally, $\vec{L} = 0$ for such an ion. In most cases, however, the orbital quenching of such an ion is incomplete, so that it has a small nonvanishing orbital momentum $\delta\vec{L}$. In general, a magnetic ion with remnant orbital momentum $\delta\vec{L}$ has a nonzero magnetic moment along all directions of the coordinate space with a certain direction energetically favored over other directions, thereby exhibiting a preferred spin orientation (see section 5).

3.1. Orbital Quantum Number of a Uniaxial Magnetic Ion. In quantum mechanics, the magnitudes of the orbital angular momentum \vec{L} and spin angular momentum \vec{S} of a magnetic ion are given by

$$\begin{aligned}|\vec{L}| &= \sqrt{L(L+1)}\hbar \\ |\vec{S}| &= \sqrt{S(S+1)}\hbar\end{aligned}\quad (14)$$

where L and S are the orbital and spin quantum numbers of the magnetic ion, respectively. The L value of a transition-metal magnetic ion at a certain coordinate site is determined by how its split d states are occupied and the S value by how many singly occupied d states the ion has (namely, half the number of singly occupied d states). The d-state splitting of a magnetic ion depends on the symmetry of the ion site and also on the crystal field exerted on the ion from its ligands. The pattern of the d-state splitting is commonly obtained either by considering the crystal field that the ligand atoms L exert on M as point charges⁴⁹ or by performing one-electron electronic structure calculations using extended Hückel tight-binding calculations⁵⁰ in which electron–electron repulsion is neglected. Figure 6 depicts the d-state split patterns of a linear ML_2 , a ML_6 trigonal prism, and a ML_6 octahedron expected from the crystal-field consideration. Here the coordinate z axis is chosen along the rotational axis for the linear ML_2 and ML_6 trigonal prisms and along one 3-fold rotational axis for the ML_6 octahedron.

To illustrate how the L value of the uniaxial magnetic ion in a ML_n complex is related to its electron configuration, we con-

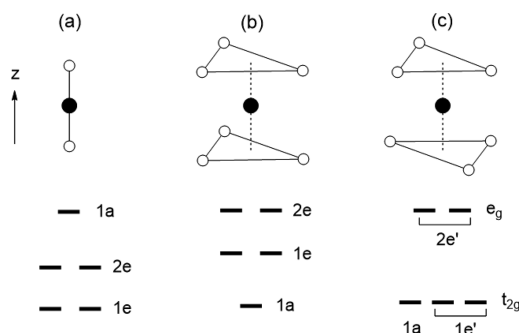


Figure 6. Split d states of ML_n expected from crystal-field considerations: (a) linear ML_2 ; (b) ML_6 trigonal prism; (c) ML_6 octahedron with the z axis taken along a 3-fold rotational axis.

sider linear ML_2 as an example. The crystal-field consideration shows that the d states of linear ML_2 are split and increase their energies as

$$\{xy, x^2 - y^2\} < \{xz, yz\} < \{3z^2 - r^2\}$$

For simplicity, we use the notations 1e, 2e, and 1a to refer to the $\{xy, x^2 - y^2\}$, $\{xz, yz\}$, and $\{3z^2 - r^2\}$ sets, respectively. The latter, in turn, are equivalent to the $\{|2, -2\rangle, |2, +2\rangle\}$, $\{|2, -1\rangle, |2, +1\rangle\}$, and $\{|2, 0\rangle\}$ sets, respectively.

$$1e \leftrightarrow \{xy, x^2 - y^2\} \leftrightarrow \{|2, -2\rangle, |2, +2\rangle\}$$

$$2e \leftrightarrow \{xz, yz\} \leftrightarrow \{|2, -1\rangle, |2, +1\rangle\}$$

$$1a \leftrightarrow \{3z^2 - r^2\} \leftrightarrow \{|2, 0\rangle\}$$

Three electron configurations that the high-spin Fe^{2+} (d^6 , $S = 2$) ion of linear ML_2 can have are depicted in Figure 7a–c. The L values for the high-spin Fe^{2+} (d^6 , $S = 2$) ion in the three configurations are given by the sum of the L_z values of the occupied $|L, L_z\rangle$ states. Therefore, we obtain

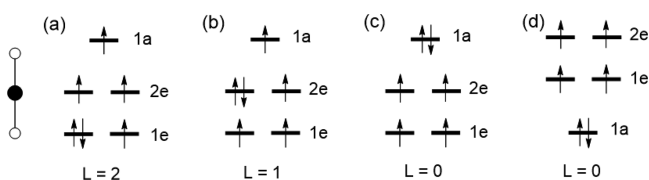


Figure 7. Configurations of linear FeL_2 containing a high-spin Fe^{2+} (d^6 , $S = 2$) ion using the d-state split pattern of $1e < 2e < 1a$: (a) $L = 2$ configuration; (b) $L = 1$ configuration; (c) $L = 0$ configuration. With the d-state split pattern of $1a < 1e < 2e$, one obtains the $L = 0$ configuration shown in part d.

$$\begin{aligned} L = 2: & \quad (1e)^3(2e)^2(1a)^1 \\ L = 1: & \quad (1e)^2(2e)^3(1a)^1 \\ L = 0: & \quad (1e)^2(2e)^2(1a)^2 \end{aligned} \quad (15)$$

The above description is also valid for the discussion of the ML_6 trigonal prism, except that its d states are split as $1a < 1e < 2e$ (Figure 6b). If the z axis of the ML_6 octahedron is chosen along one M–L bond, the split d states of the ML_6 octahedron are grouped into the t_{2g} $\{xz, yz, xy\}$, and e_g $\{x^2 - y^2, 3z^2 - r^2\}$ sets. When the geometry of the ML_6 octahedron is slightly distorted while retaining a 3-fold rotational symmetry, it is more convenient to take the z axis of the

ML_6 octahedron along its 3-fold rotational axis, as depicted in Figure 6c. Then, the t_{2g} set is described by $\{1a, 1e'\}$ and the e_g set by $\{2e'\}$,⁵¹ where

$$\begin{aligned} 1a &= 3z^2 - r^2 \\ \{1e'\} &= \left\{ \sqrt{\frac{2}{3}}xy - \sqrt{\frac{1}{3}}xz, \sqrt{\frac{2}{3}}(x^2 - y^2) - \sqrt{\frac{1}{3}}yz \right\} \\ \{2e'\} &= \left\{ \sqrt{\frac{1}{3}}xy + \sqrt{\frac{2}{3}}xz, \sqrt{\frac{1}{3}}(x^2 - y^2) + \sqrt{\frac{2}{3}}yz \right\} \end{aligned} \quad (16)$$

The $1e'$ state is composed of the $\{xy, x^2 - y^2\}$ and $\{xz, yz\}$ sets in the weight ratio of 2:1 and, hence, the $|2, \pm 2\rangle$ and $|2, \pm 1\rangle$ sets in the weight ratio of 2:1. The degeneracy between the 1a and $1e'$ states is lifted when the ML_6 octahedron distorts while retaining a 3-fold rotational symmetry.

3.2. Spin–Orbit-Coupled States. In general, one can obtain the energy spectrum of an ML_n complex using the Hamiltonian $\hat{H} = \hat{H}_{CF} + \hat{H}_{SO}$, where \hat{H}_{CF} and \hat{H}_{SO} are the crystal-field and spin–orbit operators, respectively. In the present discussion, we are concerned only with whether a magnetic ion at a certain coordination site has uniaxial magnetism or not. Then, it is sufficient to find the ground state of its spin–orbit-coupled states. In the quantum-mechanical description, the SOC of a magnetic ion is described by

$$\hat{H}_{SO} = \lambda \hat{S} \cdot \hat{L} \quad (17)$$

The ground state of this Hamiltonian is readily obtained using the classical description of SOC (eq 13) and the quantum-mechanical description of $|\vec{L}|$ and spin angular momentum $|\vec{S}|$ (eq 14). For a magnetic ion with more-than-half-occupied d states (i.e., $\lambda < 0$), its ground state is described by the largest total angular momentum quantum number, namely, by $J = L + S$. For example, for the high-spin Fe^{2+} (d^6 , $S = 2$) ion at a linear coordination site in the $L = 2$ electron configuration, the ground state is described by $J = L + S = 2 + 2 = 4$. This $J = 4$ state consists of five substates, $|J, \pm J_z\rangle$, namely, $|4, \pm 4\rangle$, $|4, \pm 3\rangle$, $|4, \pm 2\rangle$, $|4, \pm 1\rangle$, and $|4, 0\rangle$. Among these substates, the doublet, $|4, \pm 4\rangle$, is the lowest-energy state. (This is verified after evaluation of the matrix representation of the Hamiltonian $\hat{H} = \hat{H}_{CF} + \hat{H}_{SO}$ in terms of the orbital-spin basis $|L, L_z\rangle|S, S_z\rangle$ and its subsequent diagonalization. Here $L = S = 2$, and L_z and $S_z = \pm 2, \pm 1$, and 0 .⁵) In general, for a uniaxial magnetic ion of ML_n with L , S , and $\lambda < 0$, the ground level of the spin–orbit-coupled states is described by $J = L + S$, which has $2J + 1$ substates $|J, \pm J_z\rangle$. The lowest-energy substate $|J, \pm J_z\rangle$ is given by the doublet $|J, \pm J\rangle$. The importance of the ground-state doublet $|J, \pm J\rangle$ is related to the quantum-mechanical description of the magnetic moment, which is nonzero if the ground-state doublet $|J, \pm J\rangle$ is split in energy by a magnetic field.⁵ The above discussion is also applicable to a magnetic ion of ML_n with L , S , and $\lambda > 0$, except that the ground state of its spin–orbit-coupled states is given by $J = L - S$.

4. CAUSE FOR UNIAXIAL MAGNETISM⁵

Uniaxial magnetic ions in condensed matter are found among the hexagonal perovskites $A_3MM'O_6$ (A = alkaline earth; M , M' = transition metals), which consists of $MM'O_6$ chains separated by A^{2+} cations. In each $MM'O_6$ chain, the MO_6 trigonal prisms alternate with the $M'O_6$ octahedra by sharing their triangular faces (Figure 8). When $M \neq M'$, the oxidation

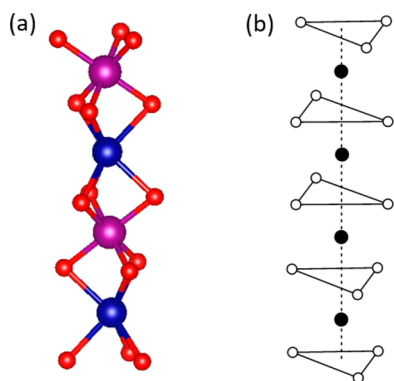


Figure 8. MM'O₆ chains present in hexagonal perovskite A₃MM'O₆ (A = alkali; M, M' = transition metals): (a) perspective view; (b) schematic view.

state of the metal is 2+ in MO₆ trigonal prisms and 4+ in M'O₆ octahedra.⁷ When M = M', as found for Ca₃Co₂O₆, the oxidation state of the metal is 3+ in both CoO₆ trigonal prisms and CoO₆ octahedra.^{52–54} Uniaxial magnetism is found for the high-spin Co³⁺ (d⁶, *S* = 2) ions of the CoO₆ trigonal prisms in Ca₃Co₂O₆^{55,56} and the high-spin Co²⁺ (d⁷, *S* = 3/2) ions of the CoO₆ trigonal prisms in Ca₃CoMnO₆,^{11,12} Ca₃CoPtO₆,^{7,13} and Sr₃CoPtO₆,^{7,13} as well as the high-spin Rh²⁺ (d⁷, *S* = 3/2) ions of the RhO₆ trigonal prisms in Sr₄RhO₆^{7,13} and Sr₃CaRhO₆.^{7,13} It is also found for the high-spin Fe²⁺ (d⁶, *S* = 2) ions of the FeO₆ octahedra in BaFe₂(PO₄)₂^{20,21} as well as for the low-spin Ir⁴⁺ (d⁵, *S* = 1/2) ions of the IrO₆ octahedra in Sr₃NiIrO₆,^{8–10} Sr₄IrO₆,^{7,13} Sr₃CaIrO₆,^{7,13} and Ca₄IrO₆.^{7,13} Uniaxial magnetism in discrete systems was first reported for the linear molecule Fe[C(SiMe₃)₃]₂,^{1,2,4} which contains a high-spin Fe²⁺ ion. More recent examples include [K(crypt-222)]Fe(C(SiMe₃)₃)₂,⁵⁷ in which the linear anion [Fe(C(SiMe₃)₃)₂][–] contains a high-spin Fe⁺ (d⁷, *S* = 3/2) ion, and linear Co(C(SiMe₂ONaph)₃)₂,⁵⁷ which contains high-spin Co²⁺ (d⁷, *S* = 3/2) ion. Discrete molecules exhibiting uniaxial magnetism have been discussed under the name of single-ion magnets.^{59,60}

4.1. One-Electron Picture of Uniaxial Magnetism.⁵

This section examines the reason why a magnetic ion in an electron configuration of unevenly occupied degenerate levels becomes uniaxial. As representative examples, we investigate the high-spin Fe²⁺ (d⁶, *S* = 2) ion at linear coordination sites and then the Co²⁺ (d⁷, *S* = 3/2) ions of the CoO₆ trigonal prisms in 2H-perovskites. Our analysis is based on the split *d* states of ML_{*n*} expected from the one-electron picture.

As discussed in the previous section, the ground state of this ion in the *L* = 2 electron configuration (Figure 7a) is given by the doublet |*J*, ±*J*⟩ = |4, ±4⟩. (*J*_{*z*} = +4 arises from *L*_{*z*} = 2 and *S*_{*z*} = 2 and *J*_{*z*} = −4 from *L*_{*z*} = −2 and *S*_{*z*} = −2.) An external magnetic field \vec{H} interacts with the moment of a magnetic ion via the Zeeman operator

$$\hat{H}_Z = \mu_B (\hat{L} + 2\hat{S}) \cdot \vec{H} \quad (18)$$

To examine if the doublet states |4, +4⟩ and |4, −4⟩ interact under Zeeman interaction, it is necessary to evaluate the matrix representation of \hat{H}_Z using the doublet states |4, +4⟩ and |4, −4⟩,

$$\begin{pmatrix} \langle 4, +4 | \hat{H}_Z | 4, +4 \rangle & \langle 4, +4 | \hat{H}_Z | 4, -4 \rangle \\ \langle 4, -4 | \hat{H}_Z | 4, +4 \rangle & \langle 4, -4 | \hat{H}_Z | 4, -4 \rangle \end{pmatrix} \quad (19)$$

The diagonalization of this matrix leads to two energy levels. When the field \vec{H} is applied along the *z* axis (i.e., the *n*-fold rotational axis of ML_{*n*}) with magnitude *H*_{||}, the Zeeman operator is given by

$$\hat{H}_Z^{\parallel} = \mu_B H_{||} (\hat{L}_z + 2\hat{S}_z) \quad (20)$$

Then, the following results are obtained by using eqs 10–12

$$\begin{aligned} \langle 4, +4 | \hat{H}_Z^{\parallel} | 4, +4 \rangle &= (L_z + 2S_z) \mu_B H_{||} = 6\mu_B H_{||} \\ \langle 4, -4 | \hat{H}_Z^{\parallel} | 4, -4 \rangle &= (L_z + 2S_z) \mu_B H_{||} = -6\mu_B H_{||} \\ \langle 4, -4 | \hat{H}_Z^{\parallel} | 4, +4 \rangle &= \langle 4, +4 | \hat{H}_Z^{\parallel} | 4, -4 \rangle = 0 \end{aligned} \quad (21)$$

Thus, the diagonalization of eq 19 gives rise to two different energy levels, 6μ_B*H*_{||} and −6μ_B*H*_{||}. That is, under magnetic field *H*_{||}, the doublet state |4, ±4⟩ splits in energy by Δ*E*_{||} = 12μ_B*H*_{||} so that the high-spin Fe²⁺ ion in the *L* = 2 electron configuration (Figure 7a) has a nonzero magnetic moment along the ||*z* direction.

When the magnetic field \vec{H} is perpendicular to the *z* axis (i.e., the ⊥*z* direction) with magnitude *H*_⊥, the Zeeman operator becomes

$$\begin{aligned} \hat{H}_Z^x &= \mu_B H_{\perp} (\hat{L}_x + 2\hat{S}_x) \\ &= \mu_B H_{\perp} [(\hat{L}_+ + \hat{L}_-) + 2(\hat{S}_+ + \hat{S}_-)]/2 \end{aligned} \quad (22)$$

if this direction is the *x* direction, but

$$\begin{aligned} \hat{H}_Z^y &= \mu_B H_{\perp} (\hat{L}_y + 2\hat{S}_y) \\ &= \mu_B H_{\perp} [(\hat{L}_+ - \hat{L}_-) + 2(\hat{S}_+ - \hat{S}_-)]/2i \end{aligned} \quad (23)$$

if the direction is the *y* direction. The diagonal matrix element ⟨4, +4| \hat{H}_Z^x |4, +4⟩ is zero, because |4, +4⟩ becomes another state by the action of \hat{H}_Z^x . For a similar reason, ⟨4, −4| \hat{H}_Z^x |4, −4⟩ is zero. For any doublet |*J*, ±*J*⟩, the operator \hat{H}_Z^x cannot change |*J*, +*J*⟩ to |*J*, −*J*⟩ or |*J*, −*J*⟩ to |*J*, +*J*⟩ as long as 2*J* > 1 because the ladder operator \hat{L}_{\pm} changes the *L*_{*z*} value by ±1 (eq 10) and because the ladder operator \hat{S}_{\pm} changes the value of *S*_{*z*} by ±1 (eq 11). Consequently,

$$\langle 4, -4 | \hat{H}_Z^x | 4, +4 \rangle = \langle 4, +4 | \hat{H}_Z^x | 4, -4 \rangle = 0$$

Namely, the doublet states |4, +4⟩ and |4, −4⟩ do not interact under \hat{H}_Z^x , so their degeneracy is not lifted under the magnetic field applied along the *x* direction. Similarly, the doublet states |4, +4⟩ and |4, −4⟩ do not interact under \hat{H}_Z^y , so their degeneracy is not lifted under the magnetic field applied along the *y* direction. Because any ⊥*z* direction is a linear combination of the *x* and *y* directions, the high-spin Fe²⁺ ion has no magnetic moment along any ⊥*z* direction. In short, the high-spin Fe²⁺ (d⁶, *S* = 2) ion in the *L* = 2 electron configuration (1e)³(2e)²(1a)¹ (Figure 7a) is uniaxial. Consider now the *L* = 1 electron configuration (1e)²(2e)³(1a)¹ of the high-spin Fe²⁺ (*S* = 2) ion shown in Figure 7b. The ground state of the spin–orbit-coupled states is described by *J* = *L* + *S* = 3, so the ground doublet becomes |*J*, ±*J*⟩ = |3, ±3⟩. Because 2*J* is greater than 1, the Fe²⁺ ion in the configuration (1e)²(2e)³(1a)¹ is uniaxial. For the *L* = 0 electron configuration (1e)²(2e)²(1a)² of the high-spin Fe²⁺ (*S* = 2) ion (Figure 7c), there is no SOC and, hence, no preferred spin orientation to a first approximation. However, a small nonzero moment δ*L* may remain on a magnetic ion because of

incomplete orbital quenching, leading to a preferred spin orientation (see section 5 for further discussion).

The crystal-field consideration shows that the d states of the ML_6 trigonal prism is split into $1a < 1e < 2e$ (Figure 6b), so $L = 2$ for the ground-state electron configuration $(1a)^2(1e)^3(2e)^2$ of the Co^{2+} (d^7 , $S = 3/2$) ion (Figure 9a). For this ion, $J = L + S = 2 + 3/2 = 7/2$ and, hence, $2J > 1$, so that the Co^{2+} (d^7 , $S = 3/2$) ion is uniaxial.

In summary, for a magnetic ion of ML_n with more-than-half-occupied d states, $\lambda < 0$, and the L value of the ion can be nonzero depending on how its d states are occupied. For a magnetic ion of nonzero L and negative λ , the ground state of

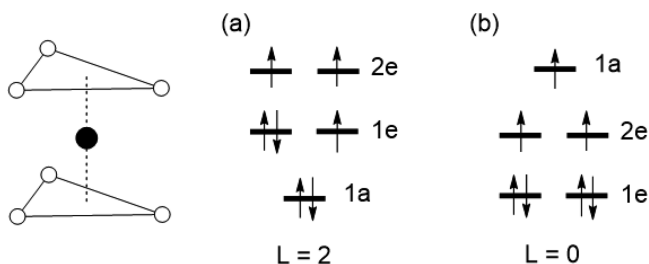


Figure 9. Configurations of the CoL_6 trigonal prism containing the high-spin Co^{2+} (d^7 , $S = 3/2$) ion: (a) $L = 2$ configuration from the d-state split pattern of $1a < 1e < 2e$; (b) $L = 0$ configuration from the d-state split pattern of $1e < 2e < 1a$.

its spin–orbit-coupled states is given by $J = L + S$ and the ground doublet by $|J, \pm J\rangle$. This magnetic ion is uniaxial if $2J > 1$. For a magnetic ion with a certain number of d electrons, more than one configuration may satisfy this condition. What matters is the lowest-energy electron configuration. Given the d-state split pattern of $1e < 2e < 1a$, the one-electron picture predicts that the $L = 2$ configuration, $(1e)^3(2e)^2(1a)^1$ (Figure 7a), is lower in energy than the $L = 1$ configuration, $(1e)^2(2e)^3(1a)^1$ (Figure 7b), and the $L = 0$ configuration, $(1e)^2(2e)^2(1a)^2$ (Figure 7c), because the total energy of a system is given by the sum of the occupied d states in this picture. The above considerations are equally valid for a magnetic ion of a less-than-half-occupied shell and an unevenly occupied degenerate level, for which $\lambda > 0$, except that the ground state of the spin–orbit-coupled states is given by $J = L - S$. In this case, it is possible for a magnetic ion to have $J = 1/2$ (e.g., $L = 1$ and $S = 1/2$) as the ground state and, hence, have no uniaxial magnetism.

4.2. Conceptual Impasse Arising from the One-Electron Picture. The high-spin Fe^+ (d^7 , $S = 3/2$) ion at the linear coordination site of the linear anion $[Fe(C(SiMe_3)_3)_2]^-$ in $[K(\text{crypt-222})]Fe(C(SiMe_3)_3)_2$ is uniaxial⁵⁷ and so is the high-spin Co^{2+} (d^7 , $S = 3/2$) ion in $Co(C(SiMe_2ONaph)_3)_2$.⁵⁸ Given the d-state split pattern of $1e < 2e < 1a$ for linear ML_2 , the one-electron picture cannot explain the uniaxial magnetism of the Fe^+ (d^7 , $S = 3/2$) ion because its ground state becomes the $L = 0$ electron configuration, $(1e)^4(2e)^2(1a)^1$ (Figure 10a). The uniaxial magnetism of the Fe^+ (d^7 , $S = 3/2$) ion was explained by adopting the $L = 2$ electron configuration, $(1a)^2(1e)^3(2e)^2$ (Figure 10b), which assumes that the d-split pattern of linear ML_2 is given by $1a < 1e < 2e$. If this is true, one cannot account for the uniaxial magnetism of the Fe^{2+} (d^6) ion at a linear coordination site because it gives rise to the $L = 0$ configuration, $(1a)^2(1e)^2(2e)^2$ (Figure 7d). Using the d-state split pattern of $1e < 2e < 1a$, one can explain neither the uniaxial magnetism of the Co^{2+} (d^7 , $S = 3/2$) ion at linear

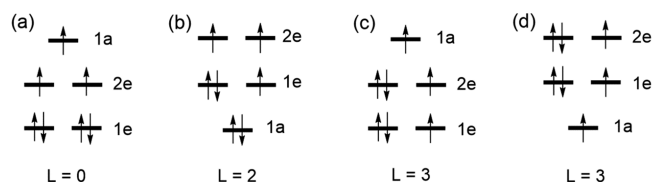


Figure 10. Configurations of linear $(FeL_2)^-$ containing the high-spin Fe^+ (d^7 , $S = 3/2$) ion: (a) $L = 0$ configuration from the d-state split pattern of $1e < 2e < 1a$; (b) $L = 2$ configuration from the d-state split pattern of $1a < 1e < 2e$. The $L = 3$ configurations of linear $(CoL_2)^0$ containing the high-spin Co^{2+} (d^7 , $S = 3/2$) ion using the d-state split patterns of (c) $1e < 2e < 1a$ and (d) $1a < 1e < 2e$.

coordination sites nor that of the Fe^+ (d^7 , $S = 3/2$) ion at linear coordination sites. The uniaxial magnetism of the Co^{2+} (d^7 , $S = 3/2$) ion was explained by adopting the $L = 3$ electron configuration, $(1e)^3(2e)^3(1a)^1$ (Figure 10c) based on the d-split pattern of $1e < 2e < 1a$, instead of using the pattern of $1a < 1e < 2e$ used for discussing the isoelectronic Fe^+ (d^7 , $S = 3/2$) ion. The $L = 3$ configuration based on the $1a < 1e < 2e$ pattern $(1a)^1(1e)^3(2e)^3$ (Figure 10d) is less stable than that of the alternative $(1e)^3(2e)^3(1a)^1$ (Figure 10c) in the one-electron picture.

In the 2H-perovskite $Ca_3Co_2O_6$, the Co^{3+} (d^6) ion of each CoO_6 octahedron is practically in the low-spin state ($\mu_S \approx 0$), and the high-spin Co^{3+} (d^6 , $S = 2$) ion of each CoO_6 trigonal prism is uniaxial.^{55,56} Given the d-state split pattern of $1a < 1e < 2e$ for the ML_6 trigonal prism (Figure 6b), the one-electron picture does not explain the uniaxial magnetism of the Co^{3+} (d^6 , $S = 2$) ion because the $L = 0$ configuration $(1a)^2(1e)^2(2e)^2$ (Figure 11a) is the ground state for the ion. To explain the

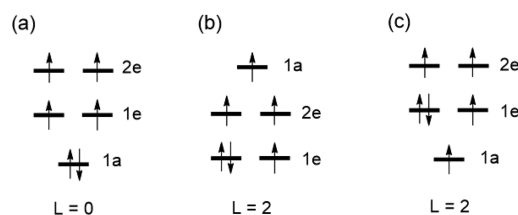


Figure 11. Configurations of the ML_6 trigonal prism containing the high-spin Co^{3+} (d^6 , $S = 2$) ion: (a) $L = 0$ configuration from the d-state split pattern of $1a < 1e < 2e$; (b) $L = 2$ configuration from the d-state split pattern of $1e < 2e < 1a$; (c) $L = 2$ configuration from the d-state split pattern of $1a < 1e < 2e$.

uniaxial magnetism of this ion, one might suppose that its split d-state pattern is given by $1e < 2e < 1a$ (Figure 11b). Then, this d-state pattern does not explain the uniaxial magnetism of the Co^{2+} (d^7 , $S = 3/2$) ion (Figure 9a), but the d-state pattern of $1a < 1e < 2e$ does (Figure 9b). This conceptual dichotomy for the ML_6 trigonal prism is similar to that discussed for linear ML_2 . Given the split d-state pattern of $1a < 1e < 2e$, the excited-state configuration $(1a)^1(1e)^3(2e)^2$ (Figure 11c) of the Co^{3+} (d^6 , $S = 2$) cation has $L = 2$ and, hence, predicts uniaxial magnetism. Thus, within the one-electron picture, the experimental observation was explained by invoking the excited-state configuration $(1a)^1(1e)^3(2e)^2$. The use of the latter was justified^{23,61} by noting that, strictly speaking, the split pattern of $1a < 1e < 2e$ is valid for an isolated ML_6 trigonal prism while, in $Ca_3Co_2O_6$, the CoO_6 trigonal prisms are not isolated. The $1a$ state (i.e., the $3z^2 - r^2$ orbital) of a CoO_6

trigonal prism overlaps strongly with that of its adjacent CoO_6 octahedra (Figure 12a) because of the short $\text{Co}\cdots\text{Co}$ distance across the shared face.

In summary, the uniaxial magnetism of the Fe^{2+} (d^6 , $S = 2$) ion is accounted for by the d-state split pattern of $1e < 2e < 1a$

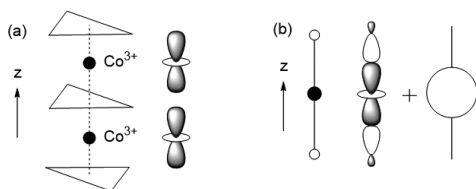


Figure 12. (a) Interaction of the $3z^2 - r^2$ orbital of a CoO_6 trigonal prism with that of its adjacent CoO_6 trigonal prism in $\text{Ca}_3\text{Co}_2\text{O}_6$ through the shared triangular face. (b) Lowering of the $1a$ level of FeL_2 by mixing of the $4s$ orbital into the $3z^2 - r^2$ orbital of Fe , hence reducing the extent of the σ antibonding in the Fe-L bonds.

(Figure 7a), but that of Fe^+ (d^7 , $S = 3/2$) ion is not (Figure 10a). The opposite is the case when the alternative split pattern $1a < 1e < 2e$ is used (Figure 10b). The uniaxial magnetism of the Fe^+ (d^7 , $S = 3/2$) ion at a linear coordination site was explained by the $1a < 1e < 2e$ pattern but that of the Co^{2+} (d^7 , $S = 3/2$) ion at a linear coordination site by the $1e < 2e < 1a$ pattern was not, despite the fact that they are isoelectronic. For linear ML_2 , the crystal-field considerations predict the d-state split pattern of $1e < 2e < 1a$, while one-electron molecular orbital calculations can show the d-state split pattern of $1a < 1e < 2e$ because the $4s$ orbital of M can mix into the $3z^2 - r^2$ orbital of M by symmetry, hence reducing the extent of the σ antibonding in the M-L bonds (Figure 12b). Regardless of which pattern is correct, it is clear that what one pattern explains contradicts what the other pattern does. To resolve this impasse, it is necessary to go beyond the one-electron picture.

4.3. Uniaxial Magnetism in the First-Principles Picture.⁶² Discrete molecules containing magnetic ions have been the subject of numerous first-principles calculations because of their spin-exchange interactions,^{63–66} spin-cross-over phenomena,^{67–70} magnetic anisotropy,^{71–73} and spin relaxation.^{73,74} In a discussion of the thermodynamic properties of a magnetic system, it is necessary to have its energy spectrum and subsequently to evaluate the Boltzmann average of the properties associated with each state of the energy spectrum. This task is commonly carried out by using a spin Hamiltonian defined in terms of a few spin-exchange parameters. The latter can be accurately determined for discrete molecules consisting of a few magnetic ions by performing elaborate configuration interaction (CI) calculations.^{63–66} For extended solids and discrete molecules composed of many magnetic ions, this CI approach becomes impracticable, so their spin-exchange parameters are evaluated by performing self-consistent-field (SCF) calculations for broken-symmetry (BS) states, namely, ordered spin states represented by one-determinant wave functions.^{38,75–80}

Each electron configuration of ML_n with an unevenly occupied degenerate d state leads to a degenerate state. If the two components of the $1e$ state, for example, are represented by $(1e_x, 1e_y)$ for simplicity, the configuration $(1e)^3(2e)^2(1a)^1$ can be described by the BS state $[(1e_x)^2(1e_y)^1](2e)^2(1a)^1$ or $[(1e_x)^1(1e_y)^2](2e)^2(1a)^1$. A qualitatively correct description of $(1e)^3(2e)^2(1a)^1$ is to employ a linear combination of $[(1e_x)^2(1e_y)^1](2e)^2(1a)^1$ and $[(1e_x)^1(1e_y)^2](2e)^2(1a)^1$, as in

complete-active-space self-consistent-field (CASSCF) calculations. Nevertheless, it was recently shown⁶² that the conceptual impasse arising from the one-electron picture is resolved at the BS level of theory, although these BS calculations do not include the static correlation effects that the CASSCF calculations provide. However, this deficiency of the BS approach is remedied, in part, by extensive CI calculations based on BS states (see below).⁶²

To probe the relative stabilities of the $L = 2, 1$, and 0 configurations (Figure 7) of the Fe^{2+} (d^6 , $S = 2$) ion at a linear coordination site as well as those of the $L = 3, 2, 1$, and 0 configurations (Figure 13) of the Fe^+ (d^7 , $S = 3/2$) and Co^{2+} (d^7 ,

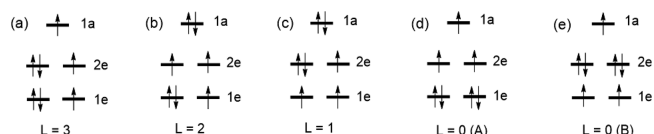


Figure 13. Configurations of linear $(\text{FeL}_2)^-$ containing the high-spin Fe^+ (d^7 , $S = 3/2$) ion and, equivalently, those of linear $(\text{CoL}_2)^0$ containing the high-spin Co^{2+} (d^7 , $S = 3/2$) ion: (a) $L = 3$ configuration; (b) $L = 2$ configuration; (c) $L = 1$ configuration; (d and e) $L = 0$ configuration.

$S = 3/2$) ions at a linear coordination site, both BS and CI calculations were carried out for linear $(\text{FeL}_2)^0$, $(\text{FeL}_2)^-$, and $(\text{CoL}_2)^0$ molecules with $L = \text{C}(\text{SiH}_3)_3$ by employing large basis sets of near Hartree–Fock accuracy plus additional polarization functions.⁶² The relative energies of the various L states of $(\text{FeL}_2)^0$, $(\text{FeL}_2)^-$, and $(\text{CoL}_2)^0$ (Figures 7 and 13), determined by SCF calculations for the BS states representing the L states, are summarized in Table 3. The three L states of $(\text{FeL}_2)^0$ increase their energies in the order $L = 2 < L = 1$ and 0 (Table 3a), and the five L states of $(\text{FeL}_2)^-$ in the order $L = 2 < L = 3, 1$, and 0 (A) $< L = 0$ (B) (Table 3b). That is, the BS calculations predict that the ground state of $(\text{FeL}_2)^0$ is the $L = 2$ state and so is that of $(\text{FeL}_2)^-$, which agrees with experiment, hence resolving the impasse that the one-electron picture creates. The five L states of $(\text{CoL}_2)^0$ increase their energies in the order $L = 2 < L = 3 < L = 0$ (A) $< L = 1$ and 0 (B) (Table 3b), showing that both $(\text{FeL}_2)^-$ and $(\text{CoL}_2)^0$ have the $L = 2$ state as the ground state.

To consider the dynamical correlation effects on the relative stabilities of various L states of $(\text{FeL}_2)^0$, $(\text{FeL}_2)^-$, and $(\text{CoL}_2)^0$,

Table 3. Relative Energies (in eV per Formula Unit) Calculated for the Various L States of $(\text{FeL}_2)^0$, $(\text{FeL}_2)^-$, and $(\text{CoL}_2)^0$, Where $L = \text{C}(\text{SiH}_3)_3$, by BS and CI Calculations

(a) (FeL ₂) ⁰						
		L = 2	L = 1	L = 0		
BS		0.00	0.17	0.26		
CI-a		0.00	0.31	0.32		
CI-b		0.00	0.30	0.32		
(b) (FeL ₂) [−] and (CoL ₂) ^{0a}						
		L = 3	L = 2	L = 1	L = 0 (A)	L = 0 (B)
BS	0.76 (0.33)	0.00 (0.00)	0.79 (1.37)	0.84 (0.57)	1.75 (1.35)	
CI-a	1.24 (0.32)	0.00 (0.00)	0.99 (1.31)	1.42 (0.65)	1.88 (1.20)	
CI-b	1.27 (0.36)	0.00 (0.00)	0.98 (1.33)	1.46 (0.64)	2.00 (1.15)	

^aThe numbers outside of parentheses are for $(\text{FeL}_2)^-$ and those in parentheses for $(\text{CoL}_2)^0$.

extensive CI calculations were carried out by transforming the virtual orbitals resulting from the SCF calculations for each BS state in two different ways:⁶² (a) The virtual orbitals are contracted by treating the molecule as a positive ion in which the 1+ charge is spread over the system (the CI-a method). (b) The virtual orbitals are localized by maximizing their exchange repulsion with the d basis functions of the transition-metal atoms (the CI-b method). The hierarchical procedure^{81–83} used for these CI calculations generate over ~100000 determinants for $(\text{FeL}_2)^0$, $(\text{FeL}_2)^-$, and $(\text{CoL}_2)^0$.⁶² Table 3 summarizes the relative energies determined for the various L states of $(\text{FeL}_2)^0$, $(\text{FeL}_2)^-$, and $(\text{CoL}_2)^0$ (Figures 7 and 13) using the CI-a and CI-b calculations. As for the relative stabilities of the three L states of $(\text{FeL}_2)^0$, the results of both CI calculations are practically identical with those of the BS calculations. Both CI calculations reveal that the energies of the five L states increase in the order $L = 2 < L = 1 < L = 3, L = 0$ (A) $< L = 0$ (B) for $(\text{FeL}_2)^-$ and in the order $L = 2 < L = 3 < L = 0$ (A) $< L = 1$ and 0 (B) for $(\text{CoL}_2)^0$. Therefore, the ground states of both $(\text{FeL}_2)^-$ and $(\text{CoL}_2)^0$ are the $L = 2$ state. The ground state of $(\text{CoL}_2)^0$ was reported to be the $L = 3$ state based on CASSCF calculations,⁷³ but details of these calculations were not given.

$(\text{FeL}_2)^-$ and $(\text{CoL}_2)^0$ are different in their first excited states, namely, the $L = 1$ state for $(\text{FeL}_2)^-$ but the $L = 3$ state for $(\text{CoL}_2)^0$. The first and second excited states are closer in energy to the ground state in $(\text{CoL}_2)^0$ than that in $(\text{FeL}_2)^-$. The first excited state lies much closer in energy to the ground state in $(\text{FeL}_2)^0$ than that in $(\text{FeL}_2)^-$. These trends reflect the fact that Fe^+ is less electronegative than Fe^{2+} and Co^{2+} and, hence, that the Fe 3d orbitals of $(\text{FeL}_2)^-$ lie higher in energy than do the Fe 3d orbitals of $(\text{FeL}_2)^0$ and the Co 3d orbitals of $(\text{CoL}_2)^0$. Thus, the d orbitals of Fe^+ are closer to the unoccupied ligand orbitals than are those of Fe^{2+} and Co^{2+} , leading to stronger metal–ligand interactions in $(\text{FeL}_2)^-$ than in $(\text{FeL}_2)^0$ and $(\text{CoL}_2)^0$.

In summary, both BS and CI calculations resolve the conceptual dilemma of the one-electron picture concerning the uniaxial magnetism of linear molecules $(\text{FeL}_2)^0$, $(\text{FeL}_2)^-$, and $(\text{CoL}_2)^0$. We note that this dilemma is resolved even at the BS level of theory, in which the total energy of an electron configuration depends on the energy sequence of the occupied d states and also on the electron repulsion between the occupied d states.

5. SELECTION RULES FOR THE PREFERRED SPIN ORIENTATION^{8,36,38}

When a magnetic ion of a ML_n complex does not fulfill the condition for uniaxial magnetism, its orbital momentum \vec{L} is mostly quenched but a small momentum, $\delta\vec{L}$, remains. There are two ways of dealing with $\delta\vec{L}$. One is to do first-principles electronic structure calculations with SOC effects included.⁸⁴ This computational approach, although brute force in nature, allows one to find the preferred directions of spins in coordinate space by calculating the total energy of a magnetic system as a function of their spin directions. The remnant orbital momentum $\delta\vec{L}$ at each magnetic ion is determined variationally as a consequence of first-principles calculations. In this approach, both the orbital and spin degrees of freedom are taken into consideration in the calculations, although not analytically. The alternative way of dealing with the remnant $\delta\vec{L}$ is noncomputational in nature. It suppresses the orbital degree of freedom completely, leading to an analytical tool,

namely, a spin-only Hamiltonian that includes the effect of SOC indirectly into the parameters defining the spin Hamiltonian.²³

In the following, we first discuss the effective spin-approximation approach to see what kinds of pictures it has generated and then develop the conceptual tools with which to analyze the results of either first-principles calculations or experimental results concerning preferred spin orientations.

5.1. Effective Spin Approximation.²³ For a single magnetic ion with remnant orbital momentum $\delta\vec{L}$, one may evaluate the effect of SOC arising from $\delta\vec{L}$ by equating the eigenvalue spectrum of its Hamiltonian expected from the use of the orbital spin basis $|L, L_z\rangle|S, S_z\rangle$ to that of the Hamiltonian obtained in terms of spin-only basis $|S', S'_z\rangle$. By doing so, one can suppress the orbital degree of freedom and discuss the energy spectrum of a magnetic system solely in terms of the spin degree of freedom, resulting in a model Hamiltonian with a few adjustable parameters to determine. However, this simplification gives rise to a serious deficiency.

Zero-Field Hamiltonian and Spin-Half Misconception. For a single magnetic ion with remnant orbital momentum $\delta\vec{L}$, one may evaluate the effect of SOC arising from $\delta\vec{L}$ by equating the eigenvalue spectrum of its Hamiltonian expected from the use of the orbital spin basis $|L, L_z\rangle|S, S_z\rangle$ to that of the Hamiltonian obtained in terms of spin-only basis $|S', S'_z\rangle$. For a magnetic ion with a nondegenerate magnetic orbital (e.g., Cu^{2+}), this effective spin approximation (i.e., the spin-only description) transforms the SOC Hamiltonian $\hat{H}_{\text{SO}} = \lambda\hat{S}\cdot\hat{L}$ (i.e., $\lambda\hat{S}\cdot\delta\hat{L}$) into the zero-field spin Hamiltonian \hat{H}_{sf}

$$\hat{H}_{\text{sf}} = D\left(\hat{S}_z^2 - \frac{1}{3}\hat{S}^2\right) + \frac{1}{2}E(\hat{S}_+\hat{S}_+ + \hat{S}_-\hat{S}_-) \quad (24)$$

where the constants D and E are related to the remnant orbital momentum $\delta\vec{L}$ as²³

$$\begin{aligned} D &\propto \lambda^2(\delta L_{\parallel} - \delta L_{\perp}) \\ E &\propto \lambda^2(\delta L_x - \delta L_y) \end{aligned} \quad (25)$$

where δL_{\parallel} and δL_{\perp} are the $\parallel z$ and $\perp z$ components of $\delta\vec{L}$, respectively, while δL_x and δL_y are the x and y components of $\delta\vec{L}$, respectively. For a magnetic ion of $S > 1/2$, the degeneracy of its $2S + 1$ substates, namely, $|S, -S+1\rangle$, $|S, -S+2\rangle$, ..., $|S, S-1\rangle$, and $|S, S\rangle$, is lifted by \hat{H}_{sf} , hence predicting that such a magnetic ion has magnetic anisotropy. This is known as single-ion anisotropy. For a $S = 1/2$ magnetic ion, its two substates, $|\uparrow\rangle = \left|\frac{1}{2}, +\frac{1}{2}\right\rangle$ and $|\downarrow\rangle = \left|\frac{1}{2}, -\frac{1}{2}\right\rangle$, do not interact under \hat{H}_{sf} , namely,

$$\left\langle \frac{1}{2}, +\frac{1}{2} \left| \hat{H}_{\text{sf}} \right| \frac{1}{2}, -\frac{1}{2} \right\rangle = 0 \quad (26)$$

This leads to the conclusion that an $S = 1/2$ ion has no magnetic anisotropy because the degeneracy of its substates is not lifted by SOC. This conclusion, a direct consequence of the simplifying assumption (i.e., the effective spin approximation), disagrees with the experimentally observed magnetic anisotropy of $S = 1/2$ ions as well as first-principles electronic structure calculations for $S = 1/2$ ions. Nevertheless, it has been believed and taught for nearly 7 decades that $S = 1/2$ ions have no single-ion anisotropy, a blind belief termed the spin- $1/2$ misconception (or spin- $1/2$ syndrome).^{36,38}

The effective spin approximation greatly simplifies the description of the energy spectrum of a magnetic system by using only the spin degree of freedom and therefore has been the tool of the trade for the practitioners of spin Hamiltonians. However, this simplification forces one to conclude the absence of magnetic anisotropy for $S = 1/2$ ions, an embarrassing failure at the very fundamental level. The aficionados of model Hamiltonians explain away the experimentally observed magnetic anisotropy of $S = 1/2$ ions as a consequence of “magnetocrystalline anisotropy” and insist that the prediction of magnetic anisotropy for $S = 1/2$ ions by first-principles electronic structure calculations, in which both the orbital and spin degrees of freedom are taken into consideration, is incorrect.³⁸ The use of the term “magnetocrystalline anisotropy” is very misleading because it suggests that a nonlocal effect causes the observed anisotropy. The SOC, $\hat{H}_{\text{SO}} = \lambda \hat{S} \cdot \hat{L}$, predicting the magnetic anisotropy of all magnetic ions including $S = 1/2$ ions, has nothing to do with interactions between different magnetic ions (i.e., nonlocal interactions).³⁸ As will be discussed below, there is no doubt from both experimental and theoretical studies that $S = 1/2$ ions have magnetic anisotropy.

g Factor. The effect of the SOC and external magnetic field on the energy of a single magnetic ion is commonly discussed by studying the deviation of the g factor from the value of 2. The three Cartesian components of the remnant orbital momentum $\delta \vec{L}$ can be written as $(\delta L_x, \delta L_y, \delta L_z)$, and those of the magnetic field \vec{H} as (H_x, H_y, H_z) . Then, in terms of the quantity $\Lambda_{\mu\mu}$ defined as

$$\Lambda_{\mu\mu} = \frac{\delta L_\mu}{2\mu_B H_\mu} \quad (27)$$

the g factor along the three directions is written as²³

$$g_\mu = 2(1 - \lambda \Lambda_{\mu\mu}) \quad (\mu = x, y, z) \quad (28)$$

where $-2\lambda \Lambda_{\mu\mu}$ is the deviation of the g factor from 2. This deviation is induced by the SOC associated with the remnant orbital angular momentum $\delta \vec{L}$; the greater $\delta \vec{L}$, the more the g factor deviates from 2. The energy change ΔE_μ under the magnetic field H_μ along the direction μ ($=x, y, z$) is proportional to the g factor g_μ . Thus, the preferred spin orientation is the direction with the largest g_μ .

Dzyaloshinskii–Moriya (DM) Exchange. For a spin dimer consisting of two equivalent magnetic ions i and j , the ion i is described by \hat{S}_i and \hat{L}_i and the ion j by \hat{S}_j and \hat{L}_j . Then, the SOC of the dimer is described by²³

$$\lambda \hat{S} \cdot \hat{L} = \lambda (\hat{S}_i + \hat{S}_j) \cdot (\hat{L}_i + \hat{L}_j) \approx \lambda \hat{S}_i \cdot \hat{L}_i + \lambda \hat{S}_j \cdot \hat{L}_j \quad (29)$$

When the orbital ground state is nondegenerate, one can obtain the second-order perturbation energy given by²³

$$[\lambda J_{ij}(\delta \vec{L}_i - \delta \vec{L}_j)] \cdot (\vec{S}_i \times \vec{S}_j) \quad (30)$$

by using the dimer SOC (eq 29) as the perturbation. Here J_{ij} is the spin exchange between the two spin sites i and j , while $\delta \vec{L}_i$ and $\delta \vec{L}_j$ are the remnant orbital angular momenta at sites i and j , respectively. Then, it is clear that the above energy is the same as the DM exchange if the $\lambda J_{ij}(\delta \vec{L}_i - \delta \vec{L}_j)$ term is identified as the DM vector \vec{D}_{ij} ,

$$\vec{D}_{ij} = \lambda J_{ij}(\delta \vec{L}_i - \delta \vec{L}_j) \quad (31)$$

In general, the sign of the parameter \vec{D}_{ij} is determined by that of the spin exchange J_{ij} and also by that of the difference $\delta \vec{L}_i - \delta \vec{L}_j$.

The DM interaction between rare-earth (RE) and transition-metal (TM) magnetic ions presents an interesting situation. By analogy with eq 31, this interaction can be written as

$$[\sqrt{\lambda_{\text{RE}} \lambda_{\text{TM}}} J_{\text{RE-TM}}(\delta \vec{L}_{\text{RE}} - \delta \vec{L}_{\text{TM}})] \cdot (\vec{S}_{\text{RE}} \times \vec{S}_{\text{TM}}) \quad (32)$$

In general, orbital quenching is much weaker for RE ions than for TM ions because the f orbitals of a RE ion do not overlap so strongly with the p orbitals of the surrounding ligands L as the d orbitals of a TM ion do. Consequently, orbital quenching is much weaker for the RE ions than for the TM ions so that the DM vector is well approximated by⁸⁵

$$\vec{D}_{\text{RE-TM}} \approx \sqrt{\lambda_{\text{RE}} \lambda_{\text{TM}}} J_{\text{RE-TM}} \delta \vec{L}_{\text{RE}} \quad (33)$$

This means that the sign of $\vec{D}_{\text{RE-TM}}$ is governed by that of the orbital moment of the RE ion, $\delta \vec{L}_{\text{RE}}$, i.e., by the nature of the occupied $4f$ states of the RE ion, as found for the Nd^{3+} (f^3) ion of NdMnAsO and for the Ce^{3+} (f^1) ion of CeMnAsO .⁸⁵

5.2. Electronic Structures of the Magnetic Systems in First-Principles Calculations. Because of electron–electron repulsion, a given state is raised in energy when it is doubly occupied. The extent of the electron–electron repulsion is partly reduced in spin-polarized electronic structure calculations because the up-spin states are allowed to differ in energy and shape from their down-spin counterparts. In regular spin-polarized DFT calculations for magnetic systems, the energy split resulting from spin-polarized electronic structure calculations is not large enough to obtain singly occupied states that are necessary for describing their magnetic insulating states. A large split between their up-spin and down-spin states, needed to correct this deficiency, can be achieved by adding the on-site repulsion U on the magnetic ions in DFT calculations. Such calculations are known as spin-polarized DFT+ U calculations.^{86,87} Alternatively, the deficiency of spin-polarized DFT calculations can be corrected by performing DFT+hybrid calculations,⁸⁸ in which the exchange–correlation functional necessary for calculations is approximated by mixing some amount, α , of the Hartree–Fock exchange potential into the DFT functional. Thus, DFT+ U calculations depend on the empirical parameter U and the DFT+hybrid calculations on the empirical parameter α . These calculations become first-principles calculations only after the values of the empirical parameters are fixed.

In spin-polarized SCF molecular orbital (SCF-MO) or electronic band structure calculations, the d states $|i\rangle$ ($i = 1, 2, 3, \dots$) of ML_n are divided into up-spin states $|\psi_i\rangle|\uparrow\rangle$ and down-spin states $|\psi_i\rangle|\downarrow\rangle$, as depicted in Figure 14. Here $|\psi_i\rangle$ represents the spatial wave function containing the information about the orbital states $|L, L_z\rangle$. The spatial function $|\psi_i\rangle$ of an up-spin state $|\psi_i\rangle|\uparrow\rangle$ differs slightly from that of its corresponding down-spin state $|\psi_i\rangle|\downarrow\rangle$ in the weights of their M d and L p orbitals, but the character of the orbital state $|L, L_z\rangle$ is the same. Given n_\uparrow as the number of occupied $|\psi_i\rangle|\uparrow\rangle$ levels and n_\downarrow that of the occupied $|\psi_i\rangle|\downarrow\rangle$ levels, the spin S of the magnetic complex ML_n is given by $S = (n_\uparrow - n_\downarrow)/2$.

To simulate the qualitative features of DFT+ U calculations using the split d states obtained from an effective one-electron

Hamiltonian, one may simply split the up-spin d states from those of the down-spin d states approximately by a certain amount.^{8,36,38} This was illustrated in Figure 14, for a high-spin ($S = 2$) d^6 ion forming a linear ML_2 and for a high-spin ($S = 3/2$) d^7 ion forming a ML_6 trigonal prism. According to the convention in which the majority and minority spin states are regarded as up-spin and down-spin states, respectively, the HOMO and LUMO levels are found among the down-spin states if the d shell is more than half-occupied but among the up-spin states if the d shell is less than half-occupied. The HOMO and LUMO levels occur between the up-spin and down-spin states when the d shell is half-occupied in a high-spin manner.

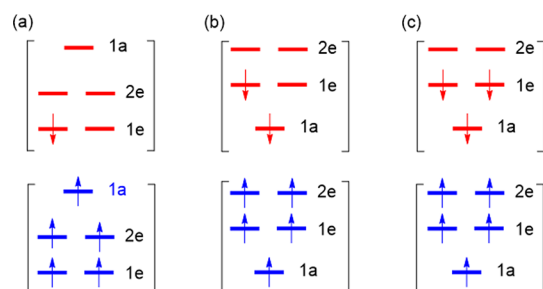


Figure 14. Spin-polarized d states simulated by separating the up-spin d states from the down-spin d states: (a) high-spin ($S = 2$) d^6 ion forming a linear ML_2 ; (b) high-spin ($S = 3/2$) d^7 ion forming a ML_6 trigonal prism; (c) high-spin Ni^{2+} ($S = 1$) d^8 ion forming a ML_6 trigonal prism.

5.3. Selection Rules for Preferred Spin Orientations.^{8,36,38}

The spin of a magnetic ion with a remnant orbital moment $\delta\vec{L}$ has a nonzero magnetic moment in all directions of the coordinate space. The energetically most favorable direction is observed experimentally at low temperature and is predicted by first-principles calculations including SOC. This direction, namely, the preferred orientation of the spin in coordinate space, is due to the SOC involving the remnant orbital momentum (i.e., $\delta\vec{L} \cdot \vec{S}$). For a magnetic ion M forming a ML_n complex with the surrounding ligands L , one can predict the preferred spin direction of M by analyzing how the HOMO and LUMO of ML_n interact under the action of the SOC, $\hat{H} = \lambda\hat{S} \cdot \hat{L}$, by using perturbation theory. To discuss this subject, one needs to analyze the selection rules governing the preferred spin orientation in terms of the HOMO–LUMO interaction induced by SOC.

As depicted in Figure 2, we use the (x, y, z) coordinate to describe the structure of ML_n with the z axis taken along the n -fold rotational axis of ML_n . This allows one to describe the orbital angular momentum \vec{L} (quantum mechanically, \hat{L}) of the magnetic ion M as already discussed. To find the preferred direction of the spin angular momentum \vec{S} (quantum mechanically, \hat{S}) of ML_n , we use another coordinate system (x', y', z') , with the z' axis taken as the observable spin direction. Then, after some manipulations, the SOC Hamiltonian $\hat{H} = \lambda\hat{S} \cdot \hat{L}$ is converted to

$$\hat{H} = \hat{H}_{SO}^0 + \hat{H}_{SO}' \quad (34)$$

where

$$\hat{H}_{SO}^0 = \lambda\hat{S}_z\left(\hat{L}_z \cos \theta + \frac{1}{2}\hat{L}_+e^{-i\phi} \sin \theta + \frac{1}{2}\hat{L}_-e^{+i\phi} \sin \theta\right) \quad (35a)$$

$$= \lambda\hat{S}_z(\hat{L}_z \cos \theta + \hat{L}_x \sin \theta \cos \phi + \hat{L}_y \sin \theta \sin \phi) \quad (35b)$$

$$\begin{aligned} \hat{H}_{SO}' = & \frac{\lambda}{2}(\hat{S}_+ + \hat{S}_-)(-\hat{L}_z \sin \theta + \hat{L}_x \cos \theta \cos \phi \\ & + \hat{L}_y \cos \theta \sin \phi) \end{aligned} \quad (36)$$

In general, the d states, $|i\rangle$ and $|j\rangle$, of ML_n interact when the matrix elements $\langle i|\hat{H}_{SO}^0|j\rangle$ and $\langle i|\hat{H}_{SO}'|j\rangle$ do not vanish. The element $\langle i|\hat{H}_{SO}^0|j\rangle$ is nonzero only when $|i\rangle$ and $|j\rangle$ have identical spins because only the terms $\langle \uparrow|\hat{S}_z|\uparrow\rangle$ and $\langle \downarrow|\hat{S}_z|\downarrow\rangle$ are nonzero. In contrast, the element $\langle i|\hat{H}_{SO}'|j\rangle$ is nonzero only when $|i\rangle$ and $|j\rangle$ have opposite spins because only the terms $\langle \uparrow|\hat{S}_+|\downarrow\rangle$ and $\langle \downarrow|\hat{S}_-|\uparrow\rangle$ are nonzero. As already mentioned, the energy associated with SOC is very small in magnitude compared with the energy split of the d states of ML_n . Therefore, the interactions among the d states $|i\rangle$ and $|j\rangle$ of ML_n induced by SOC can be analyzed by the perturbation theory with the SOC (written as in eqs 35 and 36) taken as the perturbation. Energy lowering from these interactions occurs when occupied states interact with unoccupied states, and the most important interaction between the two occur when the HOMO of ML_n interacts with the LUMO of ML_n . Then, there are two cases to consider; the HOMO and LUMO are degenerate (Figure 15a) or nondegenerate (Figure 15b). The associated energy stabilization ΔE is given by³⁶

$$\Delta E = -\left|\langle \text{HOMO}|\hat{H}_{SO}^0|\text{LUMO}\rangle\right| \quad (e_{\text{HOMO}} = e_{\text{LUMO}}) \quad (37a)$$

$$\Delta E = -\frac{\left|\langle \text{HOMO}|\hat{H}_{SO}^0|\text{LUMO}\rangle\right|^2}{|e_{\text{HOMO}} - e_{\text{LUMO}}|} \quad (e_{\text{HOMO}} \neq e_{\text{LUMO}}) \quad (37b)$$

In general, a degenerate interaction is stronger than a non-degenerate interaction. A system with degenerate HOMO and LUMO is susceptible to JT distortion, which lifts the degeneracy if it were to take place.

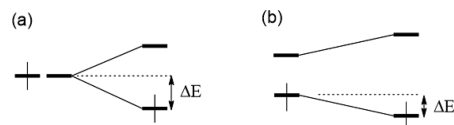


Figure 15. Energy lowering associated with the HOMO–LUMO interaction induced by SOC: (a) degenerate perturbation; (b) nondegenerate perturbation.

To determine if the preferred spin orientation is parallel to the local z direction ($\parallel z$) (of the ML_n under consideration) or perpendicular to it ($\perp z$), we note that the SOC-induced interaction between two d states, $|i\rangle$ and $|j\rangle$, is controlled by the interaction energy $\langle i|\hat{H}_{SO}|j\rangle$. For our discussion, it is necessary to find only whether or not this integral vanishes. Because the orbital/spin angular parts of the d states are expressed in terms of the products $|L, L_z\rangle|S, S_z\rangle$, the evaluation of $\langle i|\hat{H}_{SO}|j\rangle$ involves the spin integrals $\langle S, S_z'|\hat{S}_z|S, S_z\rangle$ and $\langle S, S_z'|\hat{S}_{\pm}|S, S_z\rangle$ as well as the orbital integrals $\langle L, L_z'|\hat{L}_z|L, L_z\rangle$ and $\langle L, L_z'|\hat{L}_{\pm}|L, L_z\rangle$. In the spin-polarized picture of electronic structures, $|S, S_z\rangle$ is either up-spin $|\uparrow\rangle$ or down-spin $|\downarrow\rangle$. The SOC Hamiltonian

\hat{H}_{SO}^0 contains the spin operator \hat{S}_z , so it allows interactions only between identical spin states because the only nonzero terms are $\langle \uparrow | \hat{S}_z | \uparrow \rangle$ and $\langle \downarrow | \hat{S}_z | \downarrow \rangle$. For the HOMO and LUMO of identical spin, the integral $\langle L_z | \hat{L}_z | L_z \rangle$ is nonzero if $|\Delta L_z| = 0$ between L_z' and L_z but the integral $\langle L_z | \hat{L}_z | L_z \rangle$ is nonzero if $|\Delta L_z| = 1$ between L_z' and L_z (Figure 5). Thus, according to eq 35a, we find³⁶

$$\langle \text{HOMO} | \hat{H}_{\text{SO}}^0 | \text{LUMO} \rangle \propto \begin{cases} \cos \theta, & \text{when } |\Delta L_z| = 0 \\ \sin \theta, & \text{when } |\Delta L_z| = 1 \end{cases} \quad (38)$$

For $|\Delta L_z| = 0$, the maximum value of $\langle \text{HOMO} | \hat{H}_{\text{SO}}^0 | \text{LUMO} \rangle$ occurs when $\theta = 0^\circ$. Then, the maximum energy lowering ΔE occurs when $\theta = 0^\circ$, i.e., when the spin has the $\parallel z$ orientation. If $|\Delta L_z| = 1$, the value of $\langle \text{HOMO} | \hat{H}_{\text{SO}}^0 | \text{LUMO} \rangle$ is maximum at $\theta = 90^\circ$. Thus, the maximum energy lowering ΔE occurs at $\theta = 90^\circ$, i.e., when the spin has the $\perp z$ orientation. When $|\Delta L_z| > 1$, $|i\rangle$ and $|j\rangle$ do not interact under SOC because $\langle \text{HOMO} | \hat{H}_{\text{SO}}^0 | \text{LUMO} \rangle = 0$ in such a case.

It is clear from eq 38 that the preferred spin orientation is either $\parallel z$ or $\perp z$. The preferred spin orientation can be between the $\parallel z$ and $\perp z$ directions if there are two “HOMO–LUMO” interactions such that one predicts the $\parallel z$ direction and the other the $\perp z$ direction. This situation occurs for Na_2IrO_3 .⁸

5.4. Degenerate Perturbation. This situation occurs for magnetic ions with an unevenly occupied degenerate level, namely, for uniaxial magnetic ions. In the following, we discuss the $S > 1/2$ and $S = 1/2$ cases separately.

$S > 1/2$ Ions. For the sake of completeness, we reexamine two examples of uniaxial magnetic ions in terms of perturbation theory. The HOMO and LUMO of the Fe^{2+} (d^6 , $S = 2$) ion in linear ML_2 are present in the down-spin states (Figure 14a), and so are those of the Co^{2+} (d^7 , $S = 3/2$) ion in the ML_6 trigonal prism (Figure 14b). In both cases, the HOMO and LUMO occur in the down-spin 1e set because it is singly filled, i.e.,

$$(1e \downarrow)^1 \equiv (xy \downarrow, x^2 - y^2 \downarrow)^1$$

Between the xy and $x^2 - y^2$ states, the $|\Delta L_z|$ between the HOMO and LUMO is zero, so the preferred spin orientation for both magnetic ions should be the $\parallel z$ direction in agreement with our discussion in section 4.1. As another example, consider the uniaxial magnetism that arises from the high-spin Fe^{2+} (d^6 , $S = 2$) ions in the FeO_6 octahedra of $\text{BaFe}_2(\text{PO}_4)_2$, which has honeycomb layers made up of edge-sharing FeO_6 octahedra.²⁰ For our analysis, it is convenient to choose the z axis along one 3-fold rotational axis of the ML_6 octahedron (Figure 6c). The high-spin Fe^{2+} ion has the $(t_{2g})^4(e_g)^2$ configuration, and the $(t_{2g})^4$ subconfiguration can be either the configuration $|1\rangle$ or $|2\rangle$ shown as follows (Figure 16a,b).

$$\begin{aligned} |1\rangle &\equiv (1a)^1(1e')^3 = (1a \uparrow)^1(1e' \uparrow)^2(1e' \downarrow)^1 \\ |2\rangle &\equiv (1a)^2(1e')^2 = (1a \uparrow)^1(1e' \uparrow)^2(1a \downarrow)^1 \end{aligned} \quad (39)$$

The occupancies of the down-spin d states for $|1\rangle$ and $|2\rangle$ are depicted in parts c and d of Figure 16, respectively. The SOC-induced energy lowering is strong for $|1\rangle$ because it has an unevenly occupied degenerate configuration $(1e' \downarrow)^1$, but this is not the case for $|2\rangle$ because the latter has a singly occupied nondegenerate configuration $(1a \downarrow)^1$. According to eq 17, the down-spin configuration $(1e' \downarrow)^1$ of $|1\rangle$ is expressed as

$$\begin{aligned} (1e' \downarrow)^1 &= \left(\sqrt{\frac{2}{3}} (xy \downarrow, x^2 - y^2 \downarrow)^1 - \sqrt{\frac{1}{3}} \right. \\ &\quad \left. (xz \downarrow, yz \downarrow)^1 \right) \end{aligned} \quad (40)$$

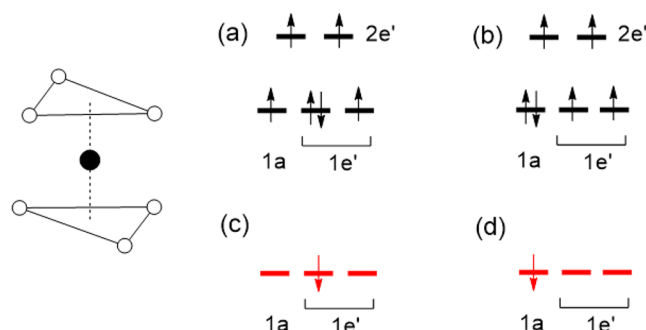


Figure 16. Two configurations of a high-spin $(t_{2g})^4(e_g)^2$ ion in the ML_6 octahedron with the z axis along a 3-fold rotational axis. They differ in their $(t_{2g})^4$ subconfigurations: (a) $(1a)^1(1e')^3$; (b) $(1a)^2(1e')^2$. The down-spin configurations corresponding to parts a and b are presented in parts c and d, respectively.

The configurations $(xy \downarrow, x^2 - y^2 \downarrow)^1$ and $(xz \downarrow, yz \downarrow)^1$ lead to $L = 2$ and 1, respectively. For configuration $|1\rangle$ of the Fe^{2+} (d^6 , $S = 2$) ion, the SOC constant $\lambda < 0$. Thus, the ground doublet has $J = L + S = 4$ from the component $(xy \downarrow, x^2 - y^2 \downarrow)^1$ ($L = 2$) and $J = 3$ from $(xz \downarrow, yz \downarrow)^1$ ($L = 1$). Because the doublet $|J, \pm J_z\rangle = |4, \pm 4\rangle$ is more stable than the doublet $|4, \pm 3\rangle$, the $(1e')^3$ configuration of the Fe^{2+} ion can be written in terms of orbital states as

$$\begin{aligned} (1e')^3 &\equiv (1e' \uparrow)^2(1e' \downarrow)^1 \\ &\Leftrightarrow (|4, +4\rangle, |4, -4\rangle)^2(|4, +3\rangle, |4, -3\rangle)^1 \end{aligned}$$

With $J_z = 3$ for the singly occupied doublet, the high-spin Fe^{2+} ion at an octahedral site is predicted to have uniaxial magnetism with $\parallel z$ spin orientation. This analysis is supported by DFT calculations, which show the orbital moment of $\sim 1 \mu_B$ (i.e., $L \approx 1$) for the Fe^{2+} ion.²¹

$S = 1/2$ Ions. $\text{Sr}_3\text{NiIrO}_6$ consists of the NiIrO_6 chains in which the IrO_6 octahedra alternate with NiO_6 trigonal prisms by sharing their triangular faces. Each NiO_6 trigonal prism has a Ni^{2+} (d^8 , $S = 1$) ion and each IrO_6 octahedron a low-spin Ir^{4+} (d^5 , $S = 1/2$) ion. According to magnetic susceptibility, magnetization, and neutron diffraction measurements,^{9,10} $\text{Sr}_3\text{NiIrO}_6$ has uniaxial magnetism, with the spins of both Ni^{2+} and Ir^{4+} ions aligned along the chain direction and the spins of adjacent Ni^{2+} and Ir^{4+} ions in each chain antiferromagnetically coupled.¹⁰ The low-spin Ir^{4+} (d^5 , $S = 1/2$) ion has the configuration $(t_{2g})^5$, which can be described by the configurations $|3\rangle$ or $|4\rangle$.

$$\begin{aligned} |3\rangle &= (1a)^2(1e')^3 \\ |4\rangle &= (1a)^1(1e')^4 \end{aligned} \quad (41)$$

The occupancies of d states for $|3\rangle$ and $|4\rangle$ are depicted in parts a and b of Figure 17, respectively. The down-spin parts of $|3\rangle$ and $|4\rangle$ are presented in parts c and d of Figure 17, respectively.

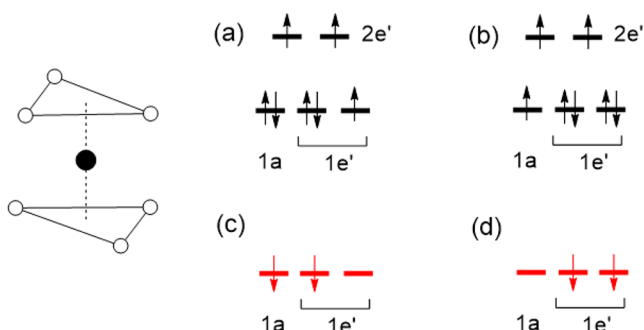


Figure 17. Two configurations of a high-spin d^7 ion in the ML_6 octahedron with the z axis along a 3-fold rotational axis: (a) $(1a)^2(1e')^3$ and (b) $(1a)^1(1e')^4$ configurations of the t_{2g} level. The down-spin configurations corresponding to parts a and b are presented in part c and d, respectively.

According to eq 16, the down-spin configuration $(1e'\downarrow)^1$ of $|1\rangle$ is expressed as in eq 40. Thus, the configuration $(xy\downarrow, x^2 - y^2\downarrow)^1$ leads to $L = 2$ and the configuration $(xz\downarrow, yz\downarrow)^1$ to $L = 1$. The SOC constant $\lambda < 0$ for the configuration $|3\rangle$ of the Ir^{4+} ($d^5, S = 1/2$) ion, so that the ground doublet is given by $J = L + S = 5/2$ from the component $(xy\downarrow, x^2 - y^2\downarrow)^1$ ($L = 2$), and $J = 3/2$ from $(xz\downarrow, yz\downarrow)^1$ ($L = 1$). Because $\lambda < 0$, the doublet $|J, \pm J_z\rangle = |5/2, \pm 5/2\rangle$ is more stable than the doublet $|5/2, \pm 3/2\rangle$, so that the $(1e')^3$ configuration of the Ir^{4+} ion is equivalent to

$$(1e')^3 \equiv (1e' \uparrow)^2 (1e' \downarrow)^1 \\ \Leftrightarrow \left(\left| \frac{5}{2}, +\frac{5}{2} \right\rangle, \left| \frac{5}{2}, -\frac{5}{2} \right\rangle \right)^2 \\ \left(\left| \frac{5}{2}, +\frac{3}{2} \right\rangle, \left| \frac{5}{2}, -\frac{3}{2} \right\rangle \right)^1$$

The singly occupied doublet has $J_z = 3/2$. This predicts uniaxial magnetism for the low-spin Ir^{4+} ion at an octahedral site with $\parallel z$ spin orientation, explaining why the $S = 1/2$ Ir^{4+} ion has a strong magnetic anisotropy with the $\parallel z$ spin direction.

Each VO_6 octahedron of $R_2V_2O_7$ (R = rare earth), containing a $S = 1/2$ V^{4+} (d^1) ion,⁸⁹ is axially compressed along the direction of its local 3-fold rotational axis. Consequently, the triply degenerate t_{2g} state (Figure 18a) of an ideal VO_6 octahedron is split into the $1a < 1e'$ pattern (Figure 18b). With the local z axis chosen along the 3-fold rotational axis of VO_6 , the $1a\uparrow$ state (i.e., the $3z^2 - r^2\uparrow$ state) becomes the HOMO and the $1e'\uparrow$ state (i.e., the $xz\uparrow$ and $yz\uparrow$ states) the LUMO. The preferred spin orientation should be $\perp z$ because $|\Delta L_z| = 1$ between the HOMO and LUMO. Experimentally, however, $\parallel z$ spin orientation was observed,⁹⁰ which was confirmed by DFT+U+SOC calculations.⁹¹ This finding is accounted for if some uniaxial magnetic character, as found for the $(1e'\uparrow)^1$ configuration of the undistorted VO_6 (Figure 18a), is present for the V^{4+} ion in the axially compressed VO_6 octahedron. The structure of each VO_6 octahedron in $R_2V_2O_7$ has a lower symmetry than an isolated, ideal VO_6 octahedron. Consequently, the true ground state for each V^{4+} ion of $R_2V_2O_7$ is mixed with some contributions of the $1e'$ and $2e'$ character

$$|1a\rangle + \gamma|1e'\rangle + \delta|2e'\rangle$$

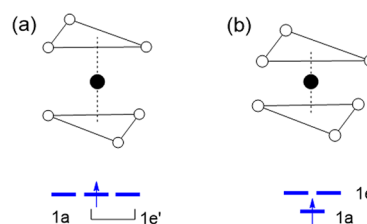


Figure 18. (a) $(t_{2g})^1$ configuration of the d^1 ion ($S = 1/2$) in a regular ML_6 octahedron, which can lead to uniaxial magnetism. (b) $(t_{2g})^1$ configuration of the d^1 ion ($S = 1/2$) in an axially compressed ML_6 octahedron, along the direction of its local 3-fold rotational axis.

where γ and δ are small mixing coefficients. Then, the configuration $(|1a\rangle + \gamma|1e'\rangle + \delta|2e'\rangle)^1$ has the $(|1e'\rangle)^1$ character responsible for the axial orientation of the V^{4+} spin in the axially compressed VO_6 octahedra in $R_2V_2O_7$.

5.5. Nondegenerate Perturbation. $S > 1/2$ Systems.

In the $NiPtO_6$ chains of Sr_3NiPtO_6 ,⁷ the NiO_6 trigonal prisms containing Ni^{2+} ($d^8, S = 1$) ions alternate with the PtO_6 octahedra containing Pt^{4+} ($d^6, S = 0$) ions by sharing their faces. For the Ni^{2+} ($d^8, S = 1$) ion, $|\Delta L_z| = 1$ because the HOMO and LUMO occur in the down-spin d states, as depicted in Figure 14c. This predicts that the preferred spin direction of the Ni^{2+} ($d^8, S = 1$) ion is $\perp z$, i.e., perpendicular to the $NiPtO_6$ chain, which agrees with first-principles calculations.⁸

The JT instability of a regular MnO_6 octahedron with a high-spin Mn^{3+} ($d^4, S = 2$) ion (Figure 19a) leads to an axially elongated MnO_6 octahedron. Such JT-distorted MnO_6 octahedra are present in $TbMnO_3$ ^{14,15} and Ag_2MnO_2 .^{16,17} The neutron diffraction studies show that the spins of the Mn^{3+} ions are aligned along the elongated Mn–O bonds.^{14,16} The LUMO is the $x^2 - y^2\uparrow$ state and the HOMO the $3z^2 - r^2\uparrow$ state (Figure 19b), given that four unpaired electrons occupy the split d states. These two states do not interact because $|\Delta L_z| = 2$ between them. The closest-lying filled d state that can interact with the LUMO is $xy\uparrow$, so the preferred spin orientation is $\parallel z$, i.e., parallel to the elongated Mn–O bonds because $|\Delta L_z| = 0$ between the two states.

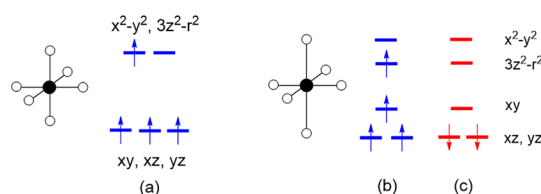


Figure 19. (a) High-spin Mn^{3+} ($d^4, S = 2$) ion in a regular MnO_6 octahedron, which leads to JT distortion. (b) High-spin Mn^{3+} ($d^4, S = 2$) ion in an axially elongated MnO_6 octahedron. (c) Low-spin Ir^{4+} ($d^5, S = 1/2$) ion in an axially elongated IrO_6 octahedron. Only the down-spin states are shown for simplicity.

Corner-sharing FeO_4 square planes containing high-spin Fe^{2+} ($d^6, S = 2$) ions are found in the FeO_2 layers of $SrFeO_2$ ^{32,33} and in two-leg ladder chains of $Sr_3Fe_2O_5$.^{34,35} The d states of a FeO_4 square plane are split, as in Figure 20, so that only the $3z^2 - r^2\downarrow$ level is occupied among the down-spin d states, with the empty $\{xz\downarrow, yz\downarrow\}$ set lying immediately above (Figure 20a). Thus, $|\Delta L_z| = 1$ between these HOMO and

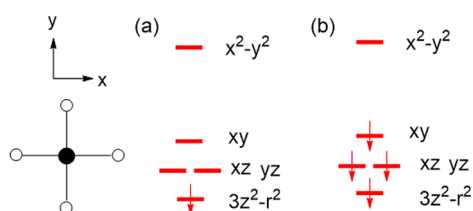


Figure 20. (a) Down-spin configuration of a high-spin Fe²⁺ (d⁶, S = 2) ion in a FeO₄ square plane of SrFeO₂. (b) Down-spin configuration of a Cu²⁺ (d⁹, S = 1/2) ion in a CuN₄ square plane in Cu(NH₃)₄SO₄·H₂O.

LUMO, predicting the preferred spin direction to be $\perp z$, i.e., parallel to the FeO₄ plane.^{33,35}

S = 1/2 Systems. The layered compound Sr₂IrO₄ consists of axially elongated IrO₆ octahedra containing low-spin Ir⁴⁺ (d⁵, S = 1/2) ions. These IrO₆ octahedra share their equatorial oxygen atoms to form IrO₄ layers, with the elongated Ir–O bonds perpendicular to the layer.^{18,19} The neutron diffraction studies show the Ir⁴⁺ spins to be parallel to the IrO₄ layer.^{18,19} When the z axis is chosen along the elongated Ir–O bond, the t_{2g} level of the IrO₆ octahedron is split into (xz, yz) < xy (Figure 19b). Given five d electrons to fill the three levels, the down-spin states xz↓ and yz↓ are filled, while the xy↓ state is empty (Figure 19c). Thus, $|\Delta L_z| = 1$ between the HOMO and LUMO, so the preferred spin direction should be $\perp z$.⁸ This prediction agrees with experiment and DFT calculations.^{8,92}

The molecular crystal CuCl₂·2H₂O consists of CuCl₂(OH₂)₂ complexes containing Cu²⁺ (d⁹, S = 1/2) ions. In each CuCl₂(OH₂)₂, the linear O–Cu–O unit is perpendicular

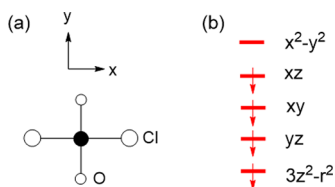


Figure 21. (a) Schematic view of CuCl₂·2H₂O, where large circles represent the chlorine atoms and small circles the H₂O molecules. The x axis is taken along the Cl–Cu–Cl bonds and the y axis along the O–Cu–O bonds. (b) Down-spin d states of CuCl₂·2H₂O.

to the linear Cl–Cu–Cl unit, as depicted in Figure 21a,²⁹ with the spins of the Cu²⁺ ions aligned along the Cu–O direction.³⁰ Thus, the Cu²⁺ ions have easy-plane anisotropy. The HOMO and LUMO of CuCl₂·2H₂O occur in the down-spin d states, with the x² – y²↓ state as the LUMO and the xz↓ state as the HOMO (Figure 21b).³¹ Because $|\Delta L_z| = 1$, the preferred spin orientation should be the $\perp z$ direction. eq 35b can be used to determine if the spin prefers the x or y direction in the xy plane. The only nonzero interaction between the x² – y²↓ and xz↓ states under SOC is the term $\langle x^2 - y^2 | \hat{L}_y | xz \rangle$ involving \hat{L}_y (see Table 3). According to eq 35b, this term comes with angular dependency of $\sin \theta \sin \phi$, which is maximized for $\theta = 90^\circ$ and $\phi = 90^\circ$. This means that the preferred spin orientation of CuCl₂(OH₂)₂ is along the y direction, namely, along the Cu–O bonds, as found experimentally.³¹

For an isolated CuL₄ square plane, the split d states are given by those found for an isolated FeO₄ square plane (Figure 20). Thus, for the Cu²⁺ (d⁹, S = 1/2) ion of the CuN₄ square plane

in Cu(NH₃)₄SO₄·H₂O,^{22,23} the down-spin d states are occupied as in Figure 20b, namely,

$$\text{isolated CuL}_4: (3z^2 - r^2 \downarrow)^1 (xz \downarrow, yz \downarrow)^2 (xy \downarrow)^1 (x^2 - y^2 \downarrow)^0 \quad (42a)$$

Because $|\Delta L_z| = 0$ between the HOMO and LUMO, the preferred spin for the Cu²⁺ ion of an isolated CuL₄ square plane is the $\parallel z$ spin orientation. For the same reason, the Cu²⁺ (d⁹, S = 1/2) ion of the CuO₄ square plane in Sr₃CuPtO₆ adopts the $\parallel z$ spin orientation.²⁴

In CuCl₂,^{25,26} CuBr₂,²⁷ and LiCuVO₄,²⁸ the square-planar CuL₄ units (L = Cl, Br, O) share their opposite edges to form CuL₂ ribbon chains (Figure 22a). In these ribbon-chain systems, the spins of the Cu²⁺ ions are found to have the $\perp z$ spin orientation. As depicted in Figure 22b, this is caused largely by the direct metal–metal bonding interactions involving the xy orbitals, which lowers the energy of the xy↓ state below the (xz↓, yz↓) state, leading to the configuration

$$\text{CuL}_2 \text{ ribbon chain}: (3z^2 - r^2 \downarrow)^1 (xy \downarrow)^1 (xz \downarrow, yz \downarrow)^2 (x^2 - y^2 \downarrow)^0 \quad (42b)$$

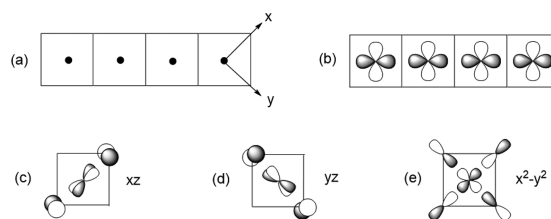


Figure 22. (a) CuL₂ (L = Cl, Br, O) ribbon chain made up of CuL₄ square planes. (b) Bonding interaction between the xy states across the shared edges of a CuL₂ ribbon chain. (c–e) xz, yz and x² – y² states.

Consequently, the interaction of the LUMO (x² – y²↓) with the HOMO (xz↓, yz↓) predicts the $\perp z$ spin orientation for the Cu²⁺ ions of the CuL₂ ribbon chains.

5.6. Exceptions to the Selection Rule? The preferred spin orientations of various magnetic ions examined so far are all explained by the selection rule based on the minimum $|\Delta L_z|$ value between their HOMO and LUMO. Among the strontium–vanadium oxide–hydrides,⁹³ two compounds apparently violate the prediction of the selection rule. The building block of these phases is the VO₄H₂ octahedron (Figure 23a) containing a V³⁺ (d², S = 1) ion, which is made up of four equatorial oxygen atoms and two apical hydrogen atoms. By sharing their apical hydrogen atoms, such VO₄H₂ octahedra form a VO₄H chain (Figure 23b). For convenience, the latter can be represented by a projection view along the chain direction, as depicted in Figure 23c. Then, the VO₃H, V₂O₃H₂, and VO₂H frameworks of the oxide–hydrides Sr₂VO₃H, Sr₃V₂O₅H₂, and SrVO₂H, respectively, result from sharing of the equatorial oxygen atoms of the VO₄H chains, as shown in Figure 24. With the local z axis of the VO₄H₂ octahedron taken along the H–V–H direction, the t_{2g} level of the V³⁺ ion is split into the (xz, yz) < xy pattern (Figure 23d). With two d electrons to fill these split d states, the minimum

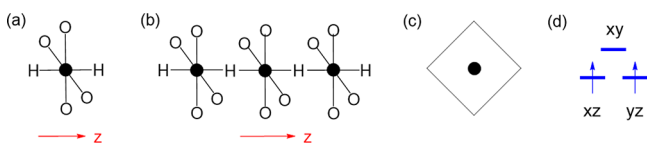


Figure 23. (a) Perspective view of a VO_4H_2 octahedron, where the vanadium atom is represented by a black circle. (b) Perspective view of a VO_3H chain formed from VO_4H_2 octahedra by sharing their apical hydrogen atoms. (c) Projection view of a VO_3H chain along the chain direction. (d) Split t_{2g} states of the V^{3+} (d^2 , $S = 1$) ion in the VO_4H_2 octahedron and their occupation with two d electrons.

$|\Delta L_z| = 1$ between the HOMO, the $(xz\uparrow, yz\uparrow)$ state, and LUMO, the $xy\uparrow$ state. Consequently, the preferred spin orientation of the V^{3+} ions should be the $\perp z$ direction in all three oxide–hydrides, $\text{Sr}_2\text{VO}_3\text{H}$, $\text{Sr}_3\text{V}_2\text{O}_5\text{H}_2$, and SrVO_2H . However, the neutron diffraction study of Romero et al.⁹³ reported that the V^{3+} spins have the $\perp z$ direction in $\text{Sr}_2\text{VO}_3\text{H}$ but the $\parallel z$ direction in $\text{Sr}_3\text{V}_2\text{O}_5\text{H}_2$ and SrVO_2H (see Figure

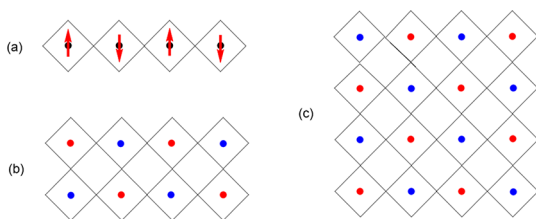


Figure 24. Reported spin orientations of the V^{3+} (d^2 , $S = 1$) ions in (a) the VO_3H framework of $\text{Sr}_2\text{VO}_3\text{H}$, (b) the $\text{V}_2\text{O}_5\text{H}_2$ framework of $\text{Sr}_3\text{V}_2\text{O}_5\text{H}_2$, and (c) the VO_2H framework of SrVO_2H . The V^{3+} (d^2 , $S = 1$) spins lie in the VO_4 square planes in $\text{Sr}_2\text{VO}_3\text{H}$ but are perpendicular to the VO_4 square planes in $\text{Sr}_3\text{V}_2\text{O}_5\text{H}_2$ and SrVO_2H . In parts b and c, the red and blue circles are used to indicate two opposite perpendicular directions of the V^{3+} spins.

24). Apparently, therefore, the spin orientation predicted for $\text{Sr}_3\text{V}_2\text{O}_5\text{H}_2$ and SrVO_2H by the selection rule is incorrect.

However, we note that the local environments of the V^{3+} ions are very similar in all three oxide–hydrides $\text{Sr}_2\text{VO}_3\text{H}$, $\text{Sr}_3\text{V}_2\text{O}_5\text{H}_2$, and SrVO_2H . The preferred spin orientation of a magnetic ion is determined largely by SOC, which is a local interaction. Consequently, there is no compelling reason why the V^{3+} spin orientations of $\text{Sr}_3\text{V}_2\text{O}_5\text{H}_2$ and SrVO_2H should differ from that of $\text{Sr}_2\text{VO}_3\text{H}$. Furthermore, the selection rule for the preferred spin orientation provides correct predictions for all other known magnetic ions. Thus, one might speculate whether the V^{3+} spin orientations of $\text{Sr}_3\text{V}_2\text{O}_5\text{H}_2$ and SrVO_2H deduced from the neutron diffraction measurements⁹³ are incorrect, whereas those predicted by the selection rule are correct. This possibility was tested by performing DFT+U+SOC calculations for $\text{Sr}_2\text{VO}_3\text{H}$, $\text{Sr}_3\text{V}_2\text{O}_5\text{H}_2$, and SrVO_2H .⁹⁴ In agreement with the prediction of the selection rule, these calculations show that the V^{3+} ions have the $\perp z$ spin orientation in all three oxide–hydrides. So far, therefore, there is no known exception to the selection rule. This points out the need to reexamine experimental results when their findings disagree with the predictions of the selection rule.

6. EFFECT OF SPIN EXCHANGE ON THE PREFERRED SPIN ORIENTATION

The energy spectrum of a magnetic system is typically obtained by employing a spin Hamiltonian. This model Hamiltonian generates the energy spectrum in terms of Heisenberg spin exchanges between spins \vec{S}_i and \vec{S}_j located at sites i and j , respectively,

$$\hat{H}_{\text{spin}} = \sum_{i < j} J_{ij} \vec{S}_i \cdot \vec{S}_j \quad (43)$$

where the constants J_{ij} (i.e., spin-exchange parameters) are the numerical parameters to determine. For example, the CuL_2 ribbon chain made up of edge-sharing CuL_4 square planes containing Cu^{2+} (d^9 , $S = 1/2$) ions is described by considering the nearest-neighbor (nn) spin exchange J_{nn} and the next-nearest-neighbor (nnn) spin exchange J_{nnn} (Figure 25a).^{27,79} The spin exchange is described by the dot product $J_{ij} \vec{S}_i \cdot \vec{S}_j$, and the preferred arrangement of the two spins \vec{S}_i and \vec{S}_j is parallel when the spin exchange is ferromagnetic (FM; i.e., $J_{ij} < 0$) but antiparallel when the spin exchange is antiferromagnetic

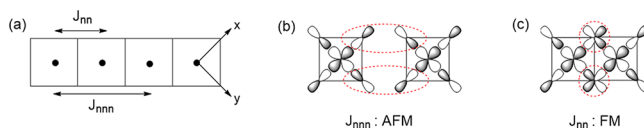


Figure 25. (a) nn and nnn spin-exchange paths of a CuL_2 ribbon chain. (b and c) Magnetic orbitals associated with the nnn and nn spin exchanges. The p-orbital tails critical for the spin exchanges are circled with dashed lines.

(AFM; i.e., $J_{ij} > 0$). In either case, the preferred spin arrangement is collinear. In the CuL_2 ribbon chain, the nnn exchange J_{nnn} is AFM (Figure 25b) because the overlap integral between the magnetic orbitals is substantial but the overlap density between the two is negligible. In contrast, the nn exchange J_{nn} of the CuL_2 ribbon is FM (Figure 25c) because the overlap integral between the magnetic orbitals is negligible but the overlap density between the two is substantial. In general, the energy scale associated with the spin exchanges between magnetic ions is much greater than that associated with the magnetic anisotropies of magnetic ions. As a result, the spin orientation at a given magnetic ion site can be influenced by the spin exchange of the magnetic site.

6.1. Between Nonequivalent Magnetic Sites. As discussed in section 5.5, the Ni^{2+} (d^8 , $S = 1$) spin \vec{S}_{Ni} of each NiO_6 trigonal prism adopts the $\perp z$ direction in $\text{Sr}_3\text{NiPtO}_6$. However, the Ni^{2+} ion of each NiO_6 trigonal prism adopts the $\parallel z$ direction in $\text{Sr}_3\text{NiIrO}_6$.¹⁰ It was shown in section 4.3 that the preferred orientation of the Ir^{4+} (d^5 , $S = 1/2$) spin \vec{S}_{Ir} at each IrO_6 octahedron adopts the $\parallel z$ direction. If the Ni^{2+} and Ir^{4+} ions were to have the spin arrangements of Figure 26a, the $\vec{S}_{\text{Ni}} \cdot \vec{S}_{\text{Ir}}$ term is zero so that there will be no energy lowering from the spin exchange $J_{\text{Ni-Ir}} \vec{S}_{\text{Ni}} \cdot \vec{S}_{\text{Ir}}$, where the spin exchange constant $J_{\text{Ni-Ir}}$ was found to be strongly AFM.⁸ It is energetically more favorable to have an AFM arrangement between the Ni^{2+} and Ir^{4+} spins (Figure 26b,c). The two AFM spin arrangements of Figure 26b,c are equivalent in energy in terms of the spin exchange $J_{\text{Ni-Ir}} \vec{S}_{\text{Ni}} \cdot \vec{S}_{\text{Ir}}$. However, the preference for

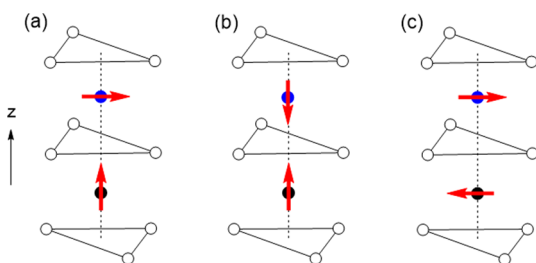


Figure 26. Three possible spin arrangements between adjacent Ni^{2+} and Ir^{4+} ions in the NiIrO_6 chains of $\text{Sr}_3\text{NiIrO}_6$, where the Ni^{2+} and Ir^{4+} ions are indicated by blue and black spheres, respectively: (a) orthogonal arrangement showing the preference for the $\perp z$ orientation of the Ni^{2+} spin and the $\parallel z$ orientation of the Ir^{4+} spin; (b) collinear AFM arrangement with the $\parallel z$ spin orientation; (c) collinear AFM arrangement with the $\perp z$ spin orientation.

the $\parallel z$ orientation of the Ir^{4+} spin arises from a degenerate perturbation but that for the $\perp z$ orientation of the Ni^{2+} spin from a nondegenerate perturbation. Therefore, the AFM arrangement based on the $\parallel z$ spin orientation is energetically more favorable, as experimentally observed for $\text{Sr}_3\text{NiPtO}_6$.

As discussed in section 5.5, the high-spin Co^{2+} (d^7 , $S = 3/2$) ions of the CoO_6 trigonal prism in $\text{Ca}_3\text{CoMnO}_6$ are uniaxial with $\parallel z$ spin orientation. The Mn^{4+} (d^3 , $S = 3/2$) ions of the MnO_6 octahedra in this compound have the $(1a\uparrow)(1e'\uparrow)^2$ configuration and hence are not expected to exhibit a strong orientation preference for their spin moments. However, the spin exchange between adjacent Co^{2+} and Mn^{4+} ions is strongly AFM, making the Mn^{4+} ions adopt the $\parallel z$ spin orientation.^{11,12}

6.2. Between Equivalent Magnetic Sites. Noncollinear Spin Arrangement as a Compromise. As a representative example, let us consider the spin arrangements of the Cu^{2+} (d^9 , $S = 1/2$) ions in a CuL_2 ribbon chain. It is known that the nnn spin exchange is AFM but the nn spin exchange is FM.^{27,79} If the spins are collinear in the CuL_2 ribbon chain, there occurs spin frustration because both the nn FM and nnn AFM spin arrangements cannot be maintained using a collinear spin arrangement. Note that the preferred spin direction of the Cu^{2+} ion in each CuL_4 square plane of the CuL_2 ribbon chain is the $\perp z$ direction, namely, any direction lying in the plane of CuL_4 . The magnitude of the nnn AFM exchange J_{nnn} is greater than that of the nn FM exchange J_{nn} , so the Cu^{2+} spins of the CuL_2 ribbon chain adopt a cycloid spin arrangement (Figure 3a); namely, the propagation direction lies in the plane of the spin rotation. A helix is obtained (Figure 3b) if the spins rotate in the planes perpendicular to the propagation direction.

Nature of the SDW and Its Implication.⁴⁸ A magnetic system with strong spin frustration does not undergo a long-range magnetic ordering.⁹⁵ In contrast, a magnetic system consisting of identical magnetic ions has the tendency to adopt a non-collinear magnetic superstructure below a certain temperature (e.g., a cycloid or a helix, as depicted in Figure 3a,b), if its spin-exchange interactions are weakly spin-frustrated.^{15,17,37,39–41}

Slightly above the onset temperature of the cycloid, a SDW state (Figure 3c,d) is often observed to occur.^{42–47} In a cycloidal or a helical structure, all moments of the ions are identical in magnitude, although they differ in orientation (Figure 3a,b). In a SDW (Figure 3c,d), however, the magnetic ions change the magnitudes of their moments depending on their positions in the crystal lattice. This is highly unphysical for any magnetic system consisting of identical magnetic ions,

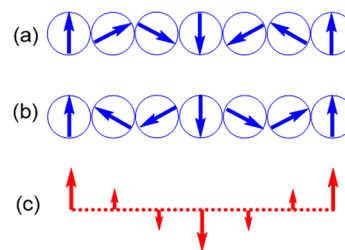


Figure 27. (a and b) Two cycloids of opposite chirality, the superposition of which gives rise to a transverse SDW shown in part c.

even though a SDW provides a mathematically correct description of the observed magnetic reflection data.

A cycloidal magnetic state is chiral in nature. Provided that the lattice of the magnetic ions is identical, therefore, a cycloid of one chirality is the same in energy as that of its opposite chirality. Consequently, the two cycloids of opposite chirality depicted in Figure 27a,b are equally populated. This produces a transversal SDW (Figure 27c) because the components of the moments along the propagation direction are canceled out,

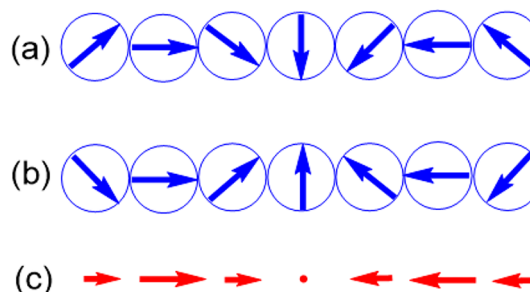


Figure 28. (a and b) Two cycloids of opposite chirality, the superposition of which gives rise to a longitudinal SDW shown in part c.

whereas those perpendicular to the propagation direction become reinforced so that their magnitudes change sinusoidally along the propagation direction. If the cycloidal states of opposite chirality shown in Figure 28a,b are equally populated, a longitudinal SDW (Figure 28c) results. In short, a SDW arises from two cycloidal states of opposite chirality when they are equally populated. The characteristic feature of a SDW, in which the magnetic ions change the magnitudes of their moments depending upon their positions in the lattice, results from equal population of the two cycloidal states of opposite chirality. The transverse (longitudinal) SDW occurs when, at a given magnetic ion site, the spin orientation prefers the direction parallel (perpendicular) to the propagation direction of the SDW.⁴⁸ Helical magnetic states are also chiral, so that a SDW can result from the superposition of two helical states of opposite chirality. Indeed, it is known that a SDW is followed by a helical magnetic state in $\text{NaFeSi}_2\text{O}_6$.⁹⁶

It should be pointed out that magnetic ions of either easy-plane or easy-axis magnetic anisotropy can give rise to cycloid states. For example, the Cu^{2+} spins of the CuL_4 square planes in the CuL_2 ($L = \text{Cl}, \text{Br}, \text{O}$) ribbon chains have the easy-plane magnetic anisotropy, and the spin rotation in the cycloid state of the CuL_2 ribbon chains takes place in the plane of the easy-plane magnetic anisotropy. The high-spin Mn^{3+} ions of the axially elongated MnO_6 octahedra in TbMnO_3 have the easy-axis magnetic anisotropy, and the plane of the spin rotation in

the cycloid state is determined by the easy-axis magnetic anisotropy and the spin exchanges between adjacent Mn^{3+} ions.^{15,48}

7. CONCLUDING REMARKS

The energy response of a magnetic ion to an external magnetic field leads to its magnetic properties, which are described by its orbital and spin angular momenta, \vec{L} and \vec{S} , respectively. These angular momenta interact with each other, leading to SOC, and also with an external magnetic field, leading to the Zeeman interaction. In the description of these interactions, it is necessary to consider the angular momenta \vec{L} and \vec{S} as quantum-mechanical operators \hat{L} and \hat{S} , respectively. In this survey, we examined the structural and electronic factors determining the preferred spin orientations of magnetic ions M in extended solids and discrete molecules. The spins of M in a complex ML_n prefers a certain direction in coordinate space because of the SOC. In general, the energy scale of SOC is very small, so elaborate experimental measurements and/or sophisticated computational efforts are required to determine the preferred spin orientations of magnetic ions. Nevertheless, the preferred spin orientations are readily predicted in terms of qualitative perturbation theory in which SOC is regarded as perturbation, namely, by analyzing the SOC-induced interactions between the HOMO and LUMO of the ML_n complexes that these magnetic ions form with their first-coordinate ligand atoms L. The orientation-dependent strengths of these HOMO–LUMO interactions are governed by the selection rules based on the minimum $|\Delta L_z|$ value between the HOMO and LUMO, namely, the $||z$ spin orientation for $|\Delta L_z| = 0$ but the $\perp z$ spin orientation for $|\Delta L_z| = 1$. These simple selection rules arise from the fact that the magnetic properties of magnetic ions are governed by the spherical harmonics $|L, L_z\rangle$ constituting their atomic orbitals and, particularly, by how the magnetic quantum numbers L_z are affected by the angular momentum operators.

AUTHOR INFORMATION

Corresponding Author

*E-mail: mike_whangbo@ncsu.edu.

ORCID

Myung-Hwan Whangbo: 0000-0002-2220-1124

Hongjun Xiang: 0000-0001-9465-5216

Author Contributions

The manuscript was written through contributions of all authors. All authors have given approval to the final version of the manuscript.

Notes

The authors declare no competing financial interest.

ACKNOWLEDGMENTS

M.H.W. would like to thank Professor Jürgen Köhler and Dr. Reinhard K. Kremer of Max-Planck-Institut für Festkörperforschung, Dr. Stéphane Jobic and Dr. Raymond Brec of Institut des Matériaux Jean Rouxel, Dr. Antoine Villesuzanne and Professor Michel Pouchat of Institut de Chimie de la Matière Condensée de Bordeaux, Professor Baibiao Huang and Professor Ying Dai of Shandong University, and Professor Shuiquan Deng of Fujian Institute of Research on the Structure of Matter not only for the invaluable discussions on various aspects of condensed matter chemistry and physics

but also for their warm hospitalities during his visits to their laboratories over the years. The work at Kyung Hee University was supported by the Basic Science Research Program through the National Research Foundation of Korea funded by the Ministry of Education (Grant NRF-2017R1D1A1B03029624).

REFERENCES

- (1) Viehhaus, T.; Schwarz, W.; Hübner, K.; Locke, K.; Weidlein, J. The variable reaction behaviour of base-free tris(trimethylsilyl)methyl lithium with trihalogenides of earth-metals and iron. *Z. Anorg. Allg. Chem.* **2001**, 627, 715–725.
- (2) Andres, H.; Bominaar, E. L.; Smith, J. M.; Eckert, N. A.; Holland, P. L.; Münck, E. Planar three-coordinate high-spin Fe-II complexes with large orbital angular momentum: Mossbauer, electron paramagnetic resonance, and electronic structure studies. *J. Am. Chem. Soc.* **2002**, 124, 3012–3025.
- (3) LaPointe, A. M. $\text{Fe}[\text{C}(\text{SiMe}_3)_3]_2$: synthesis and reactivity of a monomeric homoleptic iron(II) alkyl complex. *Inorg. Chim. Acta* **2003**, 345, 359.
- (4) Reiff, W. M.; LaPointe, A. M.; Witten, E. H. Virtual Free Ion Magnetism and the Absence of Jahn–Teller Distortion in a Linear Two-Coordinate Complex of High-Spin Iron(II). *J. Am. Chem. Soc.* **2004**, 126, 10206–10207.
- (5) Dai, D.; Whangbo, M.-H. Analysis of the uniaxial magnetic properties of high-spin d^6 ions at trigonal prism and linear two-coordinate sites: Uniaxial magnetic properties of $\text{Ca}_3\text{Co}_2\text{O}_6$ and $\text{Fe}[\text{C}(\text{SiMe}_3)_3]_2$. *Inorg. Chem.* **2005**, 44, 4407–4414.
- (6) Reiff, W. M.; Schulz, C. E.; Whangbo, M.-H.; Seo, J. I.; Lee, Y. S.; Potratz, G. R.; Spicer, C. W.; Girolami, G. S. Consequences of Rigorous Linearity for the Orbital Magnetism and Jahn–Teller Distortion Behavior of the Two-Coordinate High Spin Iron(II) Complex $\text{Fe}[\text{N}(\text{t-Bu})_2]_2$. *J. Am. Chem. Soc.* **2009**, 131, 404–405.
- (7) Zur Loye, H.-C.; Zhao, Q. B.; Bugaris, D. E.; Chance, W. M. 2H-perovskite related oxides: Synthesis, structures, and predictions. *CrystEngComm* **2012**, 14, 23–39.
- (8) Gordon, E. E.; Xiang, H. J.; Köhler, J.; Whangbo, M.-H. Spin orientations of the spin-half Ir^{4+} ions in $\text{Sr}_3\text{NiIrO}_6$, Sr_2IrO_4 and Na_2IrO_3 : Density functional, perturbation theory and Madelung potential analyses. *J. Chem. Phys.* **2016**, 144, 114706.
- (9) Lefrançois, E.; Chapon, L. C.; Simonet, V.; Lejay, P.; Khalyavin, D.; Rayaprol, S.; Sampathkumaran, E. V.; Ballou, R.; Adroja, D. T. Magnetic order in the frustrated Ising-like chain compound $\text{Sr}_3\text{NiIrO}_6$. *Phys. Rev. B: Condens. Matter Mater. Phys.* **2014**, 90, 014408.
- (10) Toth, S.; Wu, W.; Adroja, D. T.; Rayaprol, S.; Sampathkumaran, E. V. Frustrated Ising chains on the triangular lattice in $\text{Sr}_3\text{NiIrO}_6$. *Phys. Rev. B: Condens. Matter Mater. Phys.* **2016**, 93, 174422.
- (11) Choi, Y. J.; Yi, H. T.; Lee, S.; Huang, Q.; Kiryukhin, V.; Cheong, S.-W. Ferroelectricity in an Ising Chain Magnet. *Phys. Rev. Lett.* **2008**, 100, 047601.
- (12) Zhang, Y.; Xiang, H. J.; Whangbo, M.-H. Interplay between Jahn–Teller instability, uniaxial magnetism and ferroelectricity in $\text{Ca}_3\text{CoMnO}_6$. *Phys. Rev. B: Condens. Matter Mater. Phys.* **2009**, 79, 054432.
- (13) Gordon, E. E.; Koo, H.-J.; Deng, S. Q.; Köhler, J.; Whangbo, M.-H. Group of quantum bits acting as a bit using a single-domain ferromagnet of uniaxial magnetic ions. *ChemPhysChem* **2017**, 18, 2147–2150.
- (14) Blasco, J.; Ritter, C.; Garcia, J.; de Teresa, J. M.; Perez-Cacho, J.; Ibarra, M. R. Structural and magnetic study of $\text{Tb}_{1-x}\text{Ca}_x\text{MnO}_3$ perovskites. *Phys. Rev. B: Condens. Matter Mater. Phys.* **2000**, 62, S609.
- (15) Xiang, H. J.; Wei, S.-H.; Whangbo, M.-H.; Da Silva, J. L. F. Spin-Orbit Coupling and Ion Displacements in Multiferroic TbMnO_3 . *Phys. Rev. Lett.* **2008**, 101, 037209.
- (16) Ji, S.; Kan, E. J.; Whangbo, M.-H.; Kim, J.-H.; Qiu, Y.; Matsuda, M.; Yoshida, H.; Hiroi, Z.; Green, M. A.; Ziman, T.; Lee, S.-H. Orbital order and partial electronic delocalization in a triangular magnetic

metal Ag_2MnO_2 . *Phys. Rev. B: Condens. Matter Mater. Phys.* **2010**, *81*, 094421.

(17) Kan, E. J.; Xiang, H. J.; Zhang, Y.; Lee, C.; Whangbo, M.-H. Density-functional analysis of spin exchange and ferroelectric polarization in AgCrO_2 . *Phys. Rev. B: Condens. Matter Mater. Phys.* **2009**, *80*, 104417.

(18) Ye, F.; Chi, S. X.; Chakoumakos, B. C.; Fernandez-Baca, J. A.; Qi, T. F.; Cao, G. Magnetic and crystal structures of Sr_2IrO_4 : A neutron diffraction study. *Phys. Rev. B: Condens. Matter Mater. Phys.* **2013**, *87*, 140406.

(19) Lovesey, S. W.; Khalyavin, D. Strange magnetic multipoles and neutron diffraction by an iridate perovskite (Sr_2IrO_4). *J. Phys.: Condens. Matter* **2014**, *26*, 322201.

(20) Kabbour, H.; David, R.; Pautrat, A.; Koo, H.-J.; Whangbo, M.-H.; André, G.; Mentré, O. A genuine two-dimensional Ising ferromagnet $\text{BaFe}_2(\text{PO}_4)_2$ with magnetically driven reentrant transition. *Angew. Chem., Int. Ed.* **2012**, *51*, 11745–11749.

(21) Song, Y.-J.; Lee, K.-W.; Pickett, W. E. Large orbital moment and spin-orbit enabled Mott transition in the Ising Fe honeycomb lattice of $\text{BaFe}_2(\text{PO}_4)_2$. *Phys. Rev. B: Condens. Matter Mater. Phys.* **2015**, *92*, 125109.

(22) Carlson, E. H.; Spence, R. D. Paramagnetic Resonance in $\text{Cu}(\text{NH}_3)_4\text{SO}_4 \cdot \text{H}_2\text{O}$. *J. Chem. Phys.* **1956**, *24*, 471.

(23) Dai, D.; Xiang, H. J.; Whangbo, M.-H. Effects of spin-orbit coupling on magnetic properties of discrete and extended magnetic systems. *J. Comput. Chem.* **2008**, *29*, 2187–2209.

(24) Leiner, J. C.; Oh, J.; Kolesnikov, A. I.; Stone, M. B.; Le, M. D.; Kenny, E. P.; Powell, B. J.; Mourigal, M.; Gordon, E. E.; Whangbo, M.-H.; Kim, J.-W.; Cheong, S.-W.; Park, J.-G. Magnetic excitations of the Cu^{2+} quantum spin chain in $\text{Sr}_3\text{CuPtO}_6$. *Phys. Rev. B: Condens. Matter Mater. Phys.* **2018**, *97*, 104426.

(25) Banks, M. G.; Kremer, R. K.; Hoch, C.; Simon, A.; Ouladdiaf, B.; Broto, J.-M.; Rakoto, H.; Lee, C.; Whangbo, M.-H. Magnetic ordering in the frustrated Heisenberg chain system cupric chloride CuCl_2 . *Phys. Rev. B: Condens. Matter Mater. Phys.* **2009**, *80*, 024404.

(26) Zhao, L.; Hung, T.-L.; Li, C.-C.; Chen, Y.-Y.; Wu, M.-K.; Kremer, R. K.; Banks, M. G.; Simon, A.; Whangbo, M.-H.; Lee, C.; Kim, J. S.; Kim, I. G.; Kim, K. H. CuBr_2 – A New Multiferroic Material with High Critical Temperature. *Adv. Mater.* **2012**, *24*, 2469–2473.

(27) Koo, H.-J.; Lee, C.; Whangbo, M.-H.; McIntyre, G. J.; Kremer, R. K. On the Nature of the Spin Frustration in the CuO_2 Ribbon Chains of LiCuVO_4 : Crystal Structure Determination at 1.6 K, Magnetic Susceptibility Analysis, and Density Functional Evaluation of the Spin Exchange Constants. *Inorg. Chem.* **2011**, *50*, 3582–3588.

(28) Gibson, B. J.; Kremer, R. K.; Prokofiev, A. V.; Assmus, W.; McIntyre, G. J. Incommensurate antiferromagnetic order in the $S = 1/2$ quantum chain compound LiCuVO_4 . *Physica B* **2004**, *350*, E253.

(29) Brownstein, S.; Han, N. F.; Gabe, E. J.; Le Page, Y. A redetermination of the crystal structure of cupric chloride dihydrate. *Z. Kristallogr.* **1989**, *189*, 13–15.

(30) Poulis, N. J.; Hardeman, G. E. G. Nuclear magnetic resonance in an antiferromagnetic single crystal. Part I. *Physica* **1952**, *18*, 201–220.

(31) Liu, J.; Koo, H.-J.; Xiang, H. J.; Kremer, R. K.; Whangbo, M.-H. Most spin-1/2 transition-metal ions do have single ion anisotropy. *J. Chem. Phys.* **2014**, *141*, 124113.

(32) Tsujimoto, Y.; Tassel, C.; Hayashi, N.; Watanabe, T.; Kageyama, H.; Yoshimura, K.; Takano, M.; Ceretti, M.; Ritter, C.; Paulus, W. Infinite-layer iron oxide with a square-planar coordination. *Nature* **2007**, *450*, 1062–1065.

(33) Xiang, H. J.; Wei, S.-H.; Whangbo, M.-H. Origin of the Structural and Magnetic Anomalies of the Layered Compound SrFeO_2 : A Density Functional Investigation. *Phys. Rev. Lett.* **2008**, *100*, 167207.

(34) Kageyama, H.; Watanabe, T.; Tsujimoto, Y.; Kitada, A.; Sumida, Y.; Kanamori, K.; Yoshimura, K.; Hayashi, N.; Muranaka, S.; Takano, M.; Ceretti, M.; Paulus, W.; Ritter, C.; André, G. Spin Ladder Iron Oxide: $\text{Sr}_3\text{Fe}_2\text{O}_5$. *Angew. Chem., Int. Ed.* **2008**, *47*, 5740–5745.

(35) Koo, H.-J.; Xiang, H. J.; Lee, C.; Whangbo, M.-H. Effect of Magnetic Dipole–Dipole Interactions on the Spin Orientation and Magnetic Ordering of the Spin-Ladder Compound $\text{Sr}_3\text{Fe}_2\text{O}_5$. *Inorg. Chem.* **2009**, *48*, 9051–9053.

(36) Whangbo, M.-H.; Gordon, E. E.; Xiang, H. J.; Koo, H.-J.; Lee, C. Prediction of spin orientations in terms of HOMO-LUMO interactions using spin-orbit coupling as perturbation. *Acc. Chem. Res.* **2015**, *48*, 3080–3087.

(37) Xiang, H. J.; Lee, C.; Koo, H.-J.; Gong, X. G.; Whangbo, M.-H. Magnetic properties and energy-mapping analysis. *Dalton Trans.* **2013**, *42*, 823–853.

(38) Whangbo, M.-H.; Xiang, H. J. Magnetic Properties from the Perspectives of Electronic Hamiltonian: Spin Exchange Parameters, Spin Orientation and Spin-Half Misconception. In *Handbook in Solid State Chemistry, Vol. 5: Theoretical Descriptions*; Dronskowski, R., Kikkawa, S., Stein, A., Eds.; Wiley: New York, 2017, pp 285–343.

(39) Lee, C.; Kan, E. J.; Xiang, H. J.; Whangbo, M.-H. Theoretical Investigation of the Magnetic Structure and Ferroelectric Polarization of the Multiferroic Langasite $\text{Ba}_3\text{NbFe}_3\text{Si}_2\text{O}_{14}$. *Chem. Mater.* **2010**, *22*, 5290–5295.

(40) Lu, X. Z.; Whangbo, M.-H.; Dong, S.; Gong, X. G.; Xiang, H. J. Giant Ferroelectric Polarization of $\text{CaMn}_7\text{O}_{12}$ Induced by a Combined Effect of Dzyaloshinskii-Moriya Interaction and Exchange Striction. *Phys. Rev. Lett.* **2012**, *108*, 187204.

(41) Yang, J. H.; Li, Z. L.; Lu, X. Z.; Whangbo, M.-H.; Wei, S.-H.; Gong, X. G.; Xiang, H. J. Strong Dzyaloshinskii-Moriya Interaction and Origin of Ferroelectricity in Cu_2OSeO_3 . *Phys. Rev. Lett.* **2012**, *109*, 107203.

(42) Thompson, C. M.; Greedan, J. E.; Garlea, V. O.; Flacau, R.; Tan, M.; Nguyen, P.-H. T.; Wrobel, F.; Derakhshan, S. Partial Spin Ordering and Complex Magnetic Structure in BaYFeO_4 : A Neutron Diffraction and High Temperature Susceptibility Study. *Inorg. Chem.* **2014**, *53*, 1122–1127.

(43) Senff, D.; Link, P.; Hradil, K.; Hiess, A.; Regnault, L. P.; Sidis, Y.; Aliouane, N.; Argyriou, D. N.; Braden, M. Magnetic Excitations in Multiferroic TbMnO_3 : Evidence for a Hybridized Soft Mode. *Phys. Rev. Lett.* **2007**, *98*, 137206.

(44) Senff, D.; Aliouane, N.; Argyriou, D. N.; Hiess, A.; Regnault, L. P.; Link, L.; Hradil, K.; Sidis, Y.; Braden, M. Magnetic excitations in a cycloidal magnet: the magnon spectrum of multiferroic TbMnO_3 . *J. Phys.: Condens. Matter* **2008**, *20*, 434212.

(45) Prokhnenko, O.; Feyerherm, R.; Dudzik, E.; Landsgesell, S.; Aliouane, N.; Chapon, L.; Argyriou, D. Enhanced Ferroelectric Polarization by Induced Dy Spin Order in Multiferroic DyMnO_3 . *Phys. Rev. Lett.* **2007**, *98*, 057206.

(46) Sobolev, A.; Rusakov, V.; Moskvina, A.; Gapochka, A.; Belik, A.; Glazkova, I.; Akulenko, A.; Demazeau, G.; Presniakov, I. ^{57}Fe Mössbauer study of unusual magnetic structure of multiferroic 3R-AgFeO_2 . *J. Phys.: Condens. Matter* **2017**, *29*, 275803.

(47) Terada, N.; Khalyavin, D. D.; Manuel, P.; Tsujimoto, Y.; Knight, K.; Radaelli, P. G.; Suzuki, H. S.; Kitazawa, H. Spiral-Spin-Driven Ferroelectricity in a Multiferroic Delafossite AgFeO_2 . *Phys. Rev. Lett.* **2012**, *109*, 097203.

(48) Gordon, E. E.; Derakhshan, S.; Thompson, C. M.; Whangbo, M.-H. Spin-Density Wave as a Superposition of Two Magnetic States of Opposite Chirality and Its Implications. *Inorg. Chem.* **2018**, *57*, 9782–9785.

(49) Van Vleck, J. Theory of the Variations in Paramagnetic Anisotropy Among Different Salts of the Iron Group. *Phys. Rev.* **1932**, *41*, 208–215.

(50) Albright, T. A.; Burdett, J. K.; Whangbo, M.-H. *Orbital Interactions in Chemistry*, 2nd ed.; Wiley: New York, 2013.

(51) Orgel, L. E. *An Introduction to Transition Metal Chemistry*; Wiley: New York, 1969; p 174.

(52) Sampathkumaran, E. V.; Fujiwara, N.; Rayaprol, S.; Madhu, P. K.; Uwatoko, Y. Magnetic behavior of Co ions in the exotic spin-chain compound $\text{Ca}_3\text{Co}_2\text{O}_6$ from ^{59}Co NMR studies. *Phys. Rev. B: Condens. Matter Mater. Phys.* **2004**, *70*, 014437.

- (53) Hardy, V.; Lambert, S.; Lees, M. R.; Paul, D. M. Specific heat and magnetization study on single crystals of the frustrated quasi-one-dimensional oxide $\text{Ca}_3\text{Co}_2\text{O}_6$. *Phys. Rev. B: Condens. Matter Mater. Phys.* **2003**, *68*, 014424.
- (54) Whangbo, M.-H.; Dai, D.; Koo, H.-J.; Jobic, S. Investigations of the oxidation states and spin distributions in $\text{Ca}_3\text{Co}_2\text{O}_6$ and $\text{Ca}_3\text{CoRhO}_6$ by spin-polarized electronic band structure calculations. *Solid State Commun.* **2003**, *125*, 413–417.
- (55) Kageyama, H.; Yoshimura, K.; Kosuge, K.; Azuma, M.; Takano, M.; Mitamura, H.; Goto, T. Magnetic Anisotropy of $\text{Ca}_3\text{Co}_2\text{O}_6$ with Ferromagnetic Ising Chains. *J. Phys. Soc. Jpn.* **1997**, *66*, 3996.
- (56) Maignan, A.; Michel, C.; Masset, A. C.; Martin, C.; Raveau, B. Single crystal study of the one dimensional $\text{Ca}_3\text{Co}_2\text{O}_6$ compound: five stable configurations for the Ising triangular lattice. *Eur. Phys. J. B* **2000**, *15*, 657.
- (57) Zadrozny, J. M.; Xiao, D. J.; Atanasov, M.; Long, G. J.; Grandjean, F.; Neese, F.; Long, J. R. Magnetic blocking in a linear iron(I) complex. *Nat. Chem.* **2013**, *5*, 577–581.
- (58) Bunting, P. C.; Atanasov, M.; Damgaard-Møller, E.; Perfetti, M.; Crassee, I.; Orlita, M.; Overgaard, J.; van Slageren, J.; Neese, F.; Long, J. R. A linear Co(II) complex with maximal orbital angular momentum from non-Aufbau ground state. *Science* **2018**, *362*, eaat7319.
- (59) Craig, G. A.; Murrie, M. 3d single-ion magnets. *Chem. Soc. Rev.* **2015**, *44*, 2135–2147.
- (60) Frost, J. M.; Harriman, K. L. M.; Murugesu, M. The rise of 3-d single-ion magnets in molecular magnetism: towards materials from molecules? *Chem. Sci.* **2016**, *7*, 2470–2491.
- (61) Zhang, Y.; Kan, E. J.; Xiang, H. J.; Villesuzanne, A.; Whangbo, M.-H. Density functional theory analysis of the interplay between Jahn-Teller instability, uniaxial magnetism, spin arrangement, metal-metal interaction and spin-orbit coupling in Ca_3CoMO_6 ($\text{M} = \text{Co}, \text{Rh}, \text{Ir}$). *Inorg. Chem.* **2011**, *50*, 1758–1766.
- (62) Koo, H.-J.; Kasapbasi, E. E.; Whitten, J. L.; Whangbo, M.-H. Conceptual dilemma of the one-electron picture in describing the uniaxial magnetism at linear coordination sites. *Eur. J. Inorg. Chem.* **2019**, 2630–2634.
- (63) Calzado, C. J.; Cabrero, J.; Malrieu, J. P.; Caballol, R. Analysis of the magnetic coupling in binuclear complexes. I. Physics of the coupling. *J. Chem. Phys.* **2002**, *116*, 2728.
- (64) Calzado, C. J.; Cabrero, J.; Malrieu, J. P.; Caballol, R. Analysis of the magnetic coupling in binuclear complexes. II. Derivation of valence effective Hamiltonians from *ab initio* CI and DFT calculations. *J. Chem. Phys.* **2002**, *116*, 3985.
- (65) Calzado, C. J.; Angeli, C.; Taratiel, D.; Caballol, R.; Malrieu, J. P. Analysis of the magnetic coupling in binuclear systems. III. The role of the ligand to metal charge transfer excitations revisited. *J. Chem. Phys.* **2009**, *131*, 044327.
- (66) Malrieu, J. P.; Caballol, R.; Calzado, C. J.; de Graaf, C.; Guihéry, N. Magnetic Interactions in Molecules and Highly Correlated Materials: Physical Content, Analytical Derivation, and Rigorous Extraction of Magnetic Hamiltonians. *Chem. Rev.* **2014**, *114*, 429–492.
- (67) Domingo, A.; Àngels Carvajal, M.; de Graaf, C. Spin crossover in Fe(II) complexes: An *ab initio* study of ligand σ donation. *Int. J. Quantum Chem.* **2010**, *110*, 331–337.
- (68) Kepenekian, M.; Robert, V.; Le Guennic, B.; de Graaf, C. Energetics of $[\text{Fe}(\text{NCH})_6]^{2+}$ via CASPT2 calculations: A spin crossover perspective. *J. Comput. Chem.* **2009**, *30*, 2327–2333.
- (69) Kepenekian, M.; Robert, V.; Le Guennic, B. What zeroth-order Hamiltonian for CASPT2 adiabatic energetics of Fe(II)N(6) architectures? *J. Chem. Phys.* **2009**, *131*, 114702.
- (70) Suaud, N.; Bonnet, M.-L.; Boilleau, C.; Labèguerie, P.; Guihéry, N. Light-Induced Excited Spin State Trapping: *Ab Initio* Study of the Physics at the Molecular Level. *J. Am. Chem. Soc.* **2009**, *131*, 715–722.
- (71) Singh, S. K.; Rajaraman, G. Deciphering the origin of giant magnetic anisotropy and fast quantum tunnelling in Rhenium (IV) single-molecule magnets. *Nat. Commun.* **2016**, *7*, 10669.
- (72) Sarkar, A.; Velmurugan, G.; Rajeshkumar, T.; Rajaraman, G. Deciphering the origin of invariance in magnetic anisotropy in $\{\text{Fe}^{\text{II}}\text{S}_4\}$ complexes: a theoretical perspective. *Dalton Trans* **2018**, *47*, 9980–9984.
- (73) Atanasov, M.; Aravena, D.; Suturina, E.; Bill, E.; Maganas, D.; Neese, F. First principles approach to the electronic structure, magnetic anisotropy and spin relaxation in mononuclear 3d-transition metal single molecule magnets. *Coord. Chem. Rev.* **2015**, 289–290, 177–214.
- (74) Zadrozny, J. M.; Atanasov, M.; Bryan, A. M.; Lin, C.-Y.; Rekken, B. D.; Power, P. P.; Neese, F.; Long, J. R. Slow magnetization dynamics in a series of two-coordinate iron(II) complexes. *Chem. Sci.* **2013**, *4*, 125–138.
- (75) Noodleman, L. Valence bond description of antiferromagnetic coupling in transition metal dimers. *J. Chem. Phys.* **1981**, *74*, 5737.
- (76) Noodleman, L.; Davidson, E. R. Ligand spin polarization and antiferromagnetic coupling in transition metal dimers. *Chem. Phys.* **1986**, *109*, 131.
- (77) Dai, D.; Whangbo, M.-H. Spin-Hamiltonian and density functional theory descriptions of spin exchange interactions. *J. Chem. Phys.* **2001**, *114*, 2887.
- (78) Dai, D.; Whangbo, M.-H. Spin exchange interactions of a spin dimer: Analysis of broken-symmetry spin states in terms of the eigenstates of Heisenberg and Ising spin Hamiltonians. *J. Chem. Phys.* **2003**, *118*, 29.
- (79) Whangbo, M.-H.; Koo, H.-J.; Dai, D. Spin exchange interactions and magnetic structures of extended magnetic solids with localized spins: theoretical descriptions on formal, quantitative and qualitative levels. *J. Solid State Chem.* **2003**, *176*, 417–481.
- (80) Xiang, H. J.; Kan, E. J.; Wei, S.-H.; Whangbo, M.-H.; Gong, X. G. Predicting the spin-lattice order of frustrated systems from first principles. *Phys. Rev. B: Condens. Matter Mater. Phys.* **2011**, *84*, 224429.
- (81) Whitten, J. L.; Hackmeyer, M. Configuration Interaction Studies of Ground and Excited States of Polyatomic Molecules. I. The CI Formulation and Studies of Formaldehyde. *J. Chem. Phys.* **1969**, *51*, 5584.
- (82) Papas, B. N.; Whitten, J. Silver as an electron source for photodissociation of hydronium. *J. Chem. Phys.* **2011**, *135*, 204701.
- (83) Whitten, J. L.; Yang, H. Theoretical studies of surface reactions on metals. *Int. J. Quantum Chem.* **1995**, *56*, 41–47.
- (84) Kuneš, K.; Novák, P.; Schmid, R.; Blaha, P.; Schwarz, K. Electronic structure of fcc The Spin-orbit calculation with $6p_{1/2}$ local orbital extension. *Phys. Rev. B: Condens. Matter Mater. Phys.* **2001**, *64*, 153102.
- (85) Lee, C.; Kan, E. J.; Xiang, H. J.; Kremer, R. K.; Lee, S.-H.; Hiroi, Z.; Whangbo, M.-H. Spin reorientation in the square-lattice antiferromagnets RMnAsO ($\text{R} = \text{Ce}, \text{Nd}$): Density functional analysis of the spin exchange interactions between the rare-earth and transitionmetal ions. *Inorg. Chem.* **2012**, *51*, 6890–6897.
- (86) Dudarev, S. L.; Botton, G. A.; Savrasov, S. Y.; Humphreys, C. J.; Sutton, A. P. Electron-energy-loss spectra and the structural stability of nickel oxide: An LSDA+U study. *Phys. Rev. B: Condens. Matter Mater. Phys.* **1998**, *57*, 1505.
- (87) Liechtenstein, A. I.; Anisimov, V. I.; Zaanen, J. Density-functional theory and strong interactions: Orbital ordering in Mott-Hubbard insulators. *Phys. Rev. B: Condens. Matter Mater. Phys.* **1995**, *52*, R5467.
- (88) Heyd, J.; Scuseria, G. E.; Ernzerhof, M. Hybrid functionals based on a screened Coulomb potential. *J. Chem. Phys.* **2003**, *118*, 8207.
- (89) Haghighirad, A. A.; Ritter, F.; Assmus, W. Crystal Growth of $\text{A}_2\text{V}_2\text{O}_7$ ($\text{A} = \text{Y}, \text{Er}, \text{and Dy}$) Pyrochlores using High Pressure. *Cryst. Growth Des.* **2008**, *8*, 1961–1965.
- (90) Knoke, G. T.; Niazi, A.; Hill, J. M.; Johnston, D. C. Synthesis, structure, and ferromagnetism of the oxygen defect pyrochlore system $\text{Lu}_2\text{V}_2\text{O}_{7-x}$ ($x = 0.40\text{--}0.65$). *Phys. Rev. B: Condens. Matter Mater. Phys.* **2007**, *76*, 054439.

- (91) Xiang, H. J.; Kan, E. J.; Whangbo, M.-H.; Lee, C.; Wei, S.-H.; Gong, X. G. Single-ion anisotropy, Dzyaloshinskii-Moriya interaction, and negative magnetoresistance of the spin-1/2 pyrochlore $R_2V_2O_7$. *Phys. Rev. B: Condens. Matter Mater. Phys.* **2011**, *83*, 174402.
- (92) Liu, P.; Khmelevskyi, S.; Kim, B.; Marsman, M.; Li, D.; Chen, X.-Q.; Sarma, D. D.; Kresse, G.; Franchini, C. Anisotropic magnetic couplings and structure-driven canted to collinear transitions in Sr_2IrO_4 by magnetically constrained noncollinear DFT. *Phys. Rev. B: Condens. Matter Mater. Phys.* **2015**, *92*, 054428.
- (93) Denis Romero, F.; Leach, A.; Möller, J. S.; Foronda, F.; Blundell, S. J.; Hayward, M. A. Strontium Vanadium Oxide-Hydrides: “Square-Planar” Two-Electron Phases. *Angew. Chem., Int. Ed.* **2014**, *53*, 7556–7559.
- (94) Koo, H.-J.; Whangbo, M.-H. In preparation.
- (95) Greedan, J. E. Geometrically frustrated magnetic materials. *J. Mater. Chem.* **2001**, *11*, 37–53.
- (96) Baum, M. M. Neutron-Scattering Studies on Chiral Multi-ferroics. Dissertation, Universität zu Köln, Köln, Germany, 2013.